1   **Characterization of Boundary Layer Turbulent Processes by the Raman Lidar**

2   **BASIL in the frame of HD(CP)[2]) Observational Prototype Experiment**

3

4   **Paolo Di Girolamo[1], Marco Cacciani[2], Donato Summa[1], Andrea Scoccione[2], Benedetto De Rosa[1],**

5   **Andreas Behrendt[3], Volker Wulfmeyer[3]**

6

7   [1] Scuola di Ingegneria, Università degli Studi della Basilicata, Viale dell'Ateneo Lucano n. 10, 85100

8   Potenza – Italy, email: digirolamo@unibas.it

9   [2] Dipartimento di Fisica, Università di Roma "La Sapienza", Piazzale Aldo Moro, n. 2, 00100 Roma –

10   Italy, email: marco.cacciani@uniroma1.it

11   [3] Institut für Physik und Meteorologie, Universität Hohenheim, Hohenheim – Germany, email:

12   andreas.behrendt@uni-hohenheim.de, volker.wulfmeyer@uni-hohenheim.de

13

14 **Abstract**

15 Measurements carried out by the University of BASILicata Raman lidar system (*BASIL*) are reported to

16 demonstrate the capability of this instrument to characterize turbulent processes within the convective

17 boundary layer (CBL). In order to resolve the vertical profiles of turbulent variables, high resolution

18 water vapour and temperature measurements, with a temporal resolution of 10 s and a vertical

19 resolution of 90 m and 30 m, respectively, are considered. Measurements of higher-order moments of

20 the turbulent fluctuations of water vapour mixing ratio and temperature are obtained based on the

21 application of auto-covariance analyses to the water vapour mixing ratio and temperature time series.

22 The algorithms are applied to a case study (11:30-13:30 UTC, 20 April 2013) from the High Definition

23 Clouds and Precipitation for Climate Prediction (HD(CP)[2]) Observational Prototype Experiment

24 (HOPE), held in Western Germany in the spring 2013. A new correction scheme for the elastic-signal

25 leakage in the low-quantum number rotational Raman signal is applied. The noise errors are small

26 enough to derive up to fourth-order moments for both water vapour mixing ratio and temperature

27 fluctuations.

28 To the best of our knowledge, *BASIL* is the first Raman lidar with a demonstrated capability to

29 simultaneously retrieve daytime profiles of water vapour turbulent fluctuations up to the fourth order

Atmospheric
Chemistry
and Physics
Discussions

Open Access

1   throughout the atmospheric CBL, this capability being combined with the one to also measure daytime

2   profiles of temperature fluctuations up to the fourth order.

3   For the considered case study, which represents a well-mixed and quasi-stationary CBL, the mean

4   boundary layer height is found to be 1290±77 m a.g.l. Values of the integral scale for water vapour and

5   temperature fluctuations at the top of the CBL are in the range of 70-125 s and 75-225 s, respectively;

6   these values are much larger than the temporal resolution of the measurements (10 s), which testifies

7   that the temporal resolution considered for the measurements is sufficiently high to resolve turbulence

8   processes down to the inertial sub-range and consequently resolve the major part of the turbulent

9   fluctuations. Peak values of all moments are found in the interfacial layer in the proximity of the top of

10 the CBL. Specifically, water vapour and temperature second-order moment (variance) has a maximum

11 value of 0.29 g^2kg^{-2} and 0.26 K^2, respectively, water vapour and temperature third-order moment has a

12 peak value of 0.156 g^3kg^{-3} and -0.067 K^3, respectively, while water vapour and temperature fourth-order

13 moment has a maximum value of 0.28 g^4kg^{-4} and 0.24 K^4, respectively. Water vapour and temperature

14 kurtosis have values of ~3 in the entrainment zone, which indicate normally distributed humidity and

15 temperature fluctuations. Reported values of the higher-order moments result to be in good agreement

16 with previous measurements at different locations, thus providing confidence on the possibility to use

17 them for turbulence parameterization in weather and climate models.

18 In the determination of the temperature profiles, particular care was dedicated to minimize potential

19 effects associated with elastic signal leakage in the rotational Raman signals. For this purpose, a specific

20 algorithm was defined and tested to identify and remove signal leakages and to assess the residual

21 systematic uncertainty affecting temperature measurements after correction. The application of this

22 approach confirms that for the present Raman lidar system the leakage factor keeps constant with time,

23 and consequently an appropriate assessment of its constant value allows for a complete removal of the

24 leaking elastic signal from the rotational Raman lidar signals at any time (with a residual error on

25 temperature measurements after correction not exceeding 0.16 K).

26

27 **1 Introduction**

28 Water vapour and temperature are key meteorological variables playing a major role in the definition of

29 the thermodynamic state of the atmosphere (Wulfmeyer *et al.* 2015). This is particularly true in the

30 convective boundary layer, the unstably stratified boundary layer developing in the lower troposphere

31 during the day, dominated by buoyant turbulence generation as a result of strong surface solar heating

32 (Garratt, 1992). Entrainment processes at the top of the CBL are controlled by temperature (capping)

Atmospheric
Chemistry
and Physics
Open Access
Discussions
EGU

1   inversion in the interfacial layer, ultimately influencing the vertical transport of humidity in the free
2   troposphere (Mahrt 1991; Sorbjan 1996; Sullivan *et al*. 1998, Wulfmeyer *et al.* 2016). Accurate
3   measurements of water vapour and temperature from the surface to the entrainment zone at the top of
4   the CBL are therefore essential for improving weather forecasting (Dierer *et al.*, 2009), reanalyses
5   (Bengtsson *et al.*, 2004), and regional climate simulations (Milovac *et al.* 2016).

6   Measurements of higher-order moments of moisture and temperature fluctuations provide unique and
7   essential information for the characterization of turbulent processes within the convective boundary
8   layer (CBL). Water vapour and temperature variances are key variables in turbulence, convection, and
9   cloud parameterizations considered in weather and climate models (e.g., Stull, 1988; Berg and Stull,
10 2005; Gustafson and Berg, 2007). Within the CBL, water vapour variance increases with height,
11 achieving a maximum at the top of the CBL due to the mixing of moist air in the updrafts with drier air
12 from above the CBL (Wulfmeyer 1999a,b; Kiemle *et al*., 2007). The water vapour variance profile can
13 also be used to estimate the CBL height and characterize its internal structure by exploiting the tracing
14 capabilities of atmospheric water vapour (among others, Wulfmeyer *et al.*, 2010; Turner *et al.,* 2014a,b).
15 Furthermore, water vapour skewness and kurtosis are found to be characterized by an appreciable
16 vertical variability within the CBL, which changes patterns during different phases of the CBL
17 evolution (Couvreaux *et al*., 2005, 2007).

18 Atmospheric turbulent processes within the CBL have been studied for decades based on the use of in-
19 situ sensors (among others, Lenschow and Kristensen, 1985, Kalthoff *et al.*, 2011). However, lidar
20 systems, on the basis of their capability to provide high space and time resolution and accurate
21 measurements of atmospheric water vapour and temperature, have nowadays reached the level of
22 maturity needed to investigate the relevant atmospheric processes and enable measurements of turbulent
23 variables within the CBL (among others, Eberhard et at., 1989; Frehlich and Cornman, 2002). The
24 major advantage of the lidar techniques is represented by their capability to characterize turbulent
25 variables from the proximity of the surface up to interfacial layer and above. Additionally, lidar systems
26 can be operated from different platforms and, when applied from ground-based platforms, can provide
27 excellent long-term statistics. This is also necessary for reducing sampling error which are usually
28 larger for ground-based than for airborne measurements.

29 For the characterization of water vapour turbulent fluctuations, the DIAL and Raman lidar techniques
30 have demonstrated to have the time and vertical resolution, as well as the accuracy, needed to
31 characterize turbulent processes within the CBL (Wulfmeyer, 1999a,b; Kiemle *et al*., 2007; Wulfmeyer
32 *et al.*, 2010, Turner *et al.* 2014a; Muppa *et al.*, 2016). Profiles of second- to fourth-order moments of

Atmospheric
Chemistry
and Physics
Discussions

1   turbulent temperature fluctuations in the convective boundary layer have been reported for the first time

2   by Behrendt *et al.* (2015) based on the application of the rotational Raman lidar (RRL) technique

3   (Behrendt and Reichardt, 2000; Behrendt *et al.*, 2002; Di Girolamo *et al.*, 2004, 2006; Behrendt, 2005;

4   Radlach *et al.*, 2008; Hammann *et al.*, 2015a, Hammann and Behrendt, 2015). The present

5   measurements have been carried out by the Raman lidar system *BASIL*, exploiting its capability to

6   perform high-resolution and accurate measurements of atmospheric temperature and water vapour, both

7   in daytime and night-time, based on the application of the rotational and vibrational Raman lidar

8   techniques in the UV, respectively (Di Girolamo *et al.*, 2004, 2006, 2009a; 2016a, Bhawar *et al.*, 2011).

9   These measurements allow for the determination of the vertical profiles of the turbulent fluctuation of

10   these two atmospheric variables up to the fourth order throughout the atmospheric CBL in daytime with

11   limited uncertainty. Results from this system are obtained based on the application of the approach

12   introduced by Lenschow *et al.* (2000), which allows for estimating higher-order moments of turbulent

13   variables in the presence of noisy data. Measurements of water vapour turbulent fluctuations by Raman

14   lidar had been demonstrated by Wulfmeyer *et al.* (2010), based on the use of the data from the

15   Atmospheric Radiation Measurement (ARM) Raman lidar. However, these authors came to the

16   conclusion that the noise errors affecting the ARM Raman lidar water vapour mixing ratio

17   measurements for the considered case study were too large to derive fourth-order moments with

18   sufficient accuracy. Thus, to the best of our knowledge, *BASIL* is the first Raman lidar with a

19   demonstrated capability to accurately retrieve simultaneous daytime profiles of water vapour and

20   temperature turbulent fluctuations up to the fourth order throughout the atmospheric CBL. The main

21   aim of this paper is to provide a detailed characterization of the performances of the Raman lidar *BASIL*

22   and demonstrate that profiles of turbulent variables can be determined throughout the CBL with

23   sufficient accuracy. For this purpose measurements from the High Definition Clouds and Precipitation

24   for Climate Prediction (HD(CP)2) Observational Prototype Experiment (HOPE), held in Western

25   Germany in spring 2013, are considered.

26   The paper outline is the following. Section 2 provides a description of the experimental setup, with

27   details on the data processing and the error analyses; this section also describes the correction scheme

28   considerd for removing the elastic-signal leakage in the low-quantum number rotational Raman signal

29   and the uncertainties associated with this approach. Section 3 provides a brief overview on the HOPE

30   field campaign and illustrates the criteria considered for the selection of the case study; this section also

31   illustrates the the time-height cross-sections of the water vapour mixing ratio and temperature data

32   considered for the turbulence analysis, providing remarks on the meteorological conditions occurring

33   during this period. Section 4 provides a brief description of the methodology considered for the

1   turbulence analysis and illustrates the results achieved in terms of vertical profiles of turbulent variables.

2   Finally, section 5 summarizes all results and provides some indications for possible future work.

3

4   **2 Experimental setup**

5   **2.1 System Set up and derivation of mixing-ratio and temperature profiles**

6   Prior to HOPE, the University of BASILicata Raman lidar system (*BASIL*) underwent a substantial

7   upgrade aimed to improve its overall performances in terms of measurement precision and vertical and

8   temporal resolution. These setup modifications will be described in a separate forthcoming paper (Di

9   Girolamo *et al.*, 2016b). *BASIL* is a ground-based Raman lidar hosted in a transportable sea-tainer. The

10   major feature of *BASIL* is represented by its capability to perform high-resolution and accurate

11   measurements of the vertical profiles of atmospheric temperature and water vapour, both in daytime and

12   night-time, based on the application of the rotational and vibrational Raman lidar techniques in the UV

13   (Di Girolamo *et al.*, 2004, 2006, 2009a; 2016a, Bhawar *et al.*, 2011). Besides temperature and water

14   vapour, *BASIL* is also capable of providing measurements of the vertical profiles of particle backscatter

15   at 354.7, 532 and 1064 nm, particle extinction at 354.7 and 532 nm and particle depolarization at 354.7

16   and 532 nm (Griaznov *et al.*, 2007; Di Girolamo *et al.*, 2009b, 2012a, 2012b). *BASIL* is built around a

17   Nd:YAG laser source, equipped with second and third harmonic generation crystals, capable of emitting

18   pulses at 354.7 nm, 532 nm and 1064 nm, which are simultaneously transmitted in the atmosphere along

19   the zenith. The receiver includes a large-aperture telescope in Newtonian configuration, with a 45 cm

20   diameter primary mirror and a focal length of 2.1 m, and two small-aperture telescopes (50 mm

21   diameter lenses). The radiation collected by the large-aperture telescope is split into eight portions by

22   means of dichroic or partially reflecting mirrors: specifically, two portions are fed into the detection

23   channels used for temperature measurements (at 354.3 and 352.9 nm for the low- and high-quantum

24   number rotational Raman signals, $P_{LoJ}(z)$ and $P_{HiJ}(z)$, respectively), while two other portions are sent

25   to the water vapour (at 407.5 nm) and molecular nitrogen Raman channels (at 386.7 nm); corresponding

26   signals are $P_{H_2O}(z)$ and $P_{N_2}(z)$, respectively, in what follows. Another two portions of the collected

27   radiation are fed into the 354.7 and 532 nm elastic channels. A fraction of the signal entering the 354.7

28   nm channel is split into two additional portions to allow the detection of the parallel and cross-polarized

29   elastic signals, which are used for the determination particle depolarization. Signal selection is

30   performed by means of narrowband interference filters, whose specifications were defined in Di

31   Girolamo *et al.* (2004, 2009a).

Atmospheric
Chemistry
and Physics
Discussions

1   The water vapour mixing ratio m can be obtained from the power ratio of water vapour to molecular

2   nitrogen vibrational Raman signals ($m(z) = K(z) \cdot (P_{H_2O}(z)/P_{N_2}(z))$), where $K(z)$ is a calibration factor

3   obtained by multiplying several height-dependent correction terms and a height-indipendent calibration

4   term(e.g., Whiteman, 2003). The height-dependent correction terms included $K(z)$ are a differential

5   transmission term, accounting for the different atmospheric transmission by molecules and aerosols at

6   the two wavelengths corresponding the water vapour and molecular nitrogen Raman signals, and a term

7   associated with the use of narrowband interference filters and the consequent temperature dependence

8   of H_2O and N_2 Raman scattering signals selected by these filters. The height-independent calibration

9   factor is finally obtained by the multiplication of the above mentioned signal ratio by the height-

10   dependent correction terms included $K(z)$ and the comparison of this quantity with simultaneous and co-

11   located mixing ratio measurements from different sensors (e.g., from radiosondes, microwave

12   radiometers, GPS tomography, etc.).

13   Based on the application of the pure rotational Raman lidar technique, atmospheric temperature is

14   obtained from the power ratio of high-to-low quantum number rotational Raman signals $Q(T)$ through

15   the application of the analytical expression:

16   $$Q(z) = P_{HiJ}(z)/P_{LoJ}(z) = \exp(\alpha/T(z) + \beta) \qquad (1)$$

17   with α and β being two calibration constants. Thus:

18   $$T(z) = \frac{\alpha}{\ln[Q(z)] - \beta} \qquad (2)$$

19   These two calibration constants can be determined through the comparison of the lidar signal ratio with

20   simultaneous and co-located temperature measurements from different sensors (again, radiosondes,

21   microwave radiometers, GPS tomography, etc.). The above considered analytical expression relating

22   $Q(z)$ to $T(z)$ is not the only possible expression, but it is probably the simplest and implies the smallest

23   number of calibration constants. Other more complex analytical expression have been considered in

24   literature (Behrendt and Reichardt, 2000; Di Girolamo *et al.*, 2004; Behrendt *et al.*, 2015). However, the

25   systematic error associated with assuming the above calibration function to be valid for a large portion

26   of the rotational Raman spectrum is found to have a typical amplitude of 0.2 K, which is not relevant for

27   the purposes of the present study (see Wulfmeyer *et al.*, 2016 for an assessment of the effects of

28   systematic errors on turbulence measurements).

29   During HOPE, water vapour mixing ratio and temperature measurements by *BASIL* were both

30   calibrated based on the comparison with simultaneous radiosondes, which were launched from the

Atmospheric
Chemistry
and Physics
Discussions

1   nearby supersite UHOH-KIT, located in Hambach, approx. 4 km E-SE. Mean calibration coefficients

2   for both water vapour mixing ratio and temperature measurements were estimated by comparing *BASIL*

3   and radiosonde profiles for all radiosondes launched at times when *BASIL* was operating (approximately

4   60 comparisons). The comparisons were carried out in a vertical region with an extent of 1 km located

5   above the boundary layer. This selection allows for minimizing the air mass differences related to the

6   physical distance between the lidar and the radiosonde. The variability of the calibration coefficients

7   was found to be very limited throughout the duration of the filed campaign, with single calibration

8   values showing very small deviations from the mean values. For example, for what concerns water

9   vapour measurements, the standard deviation of single calibration values from the mean calibration

10   coefficient was found to not exceed 5 %.

11   As specified above, *BASIL* underwent an upgrade before HOPE which allowed for obtaining a

12   substantial improvement of the overall performances in terms of both measurement precision and

13   vertical and temporal resolution. The upgrade included a modification of the optical layout of the

14   Nd:YAG laser source, which allowed to achieve a 65 % increase of its emitted power in the UV (from

15   an original value of 6 W, single pulse energy of 300 mJ @ 20 Hz, to a final value of 10 W, with a single

16   pulse energy of 500 mJ @ 20 Hz). The upgrade also included the implementation of a new sampling

17   system (with double signal acquisition mode, i.e. both analog & digital) in some of the measurement

18   channels allowing to acquire daytime and nighttime lidar signals with a maximum vertical and temporal

19   resolution of 7.5 m and 1-10 sec, respectively. In signal pre-processing, four adjacent data points are

20   binned together to reduce statistical fluctuations of the signals, this increasing the vertical step between

21   adjacent data points to 30 m.

22

23   **2.2 Determination of noise errors**

24   In order to characterize the quality of water vapour mixing ratio and temperature measurements, an

25   accurate assessment of noise error is necessary. Noise error is quantified as the root-square of the noise

26   variance (i.e. the noise standard deviation). Profiles of noise error affecting water vapour mixing ratio

27   and temperature measurements are illustrated in figure 1. Specifically, figure 1a illustrates the water

28   vapour mixing ratio absolute error (expressed in g kg^{-1}), figure 1b illustrates the water vapour mixing

29   ratio relative error (expressed in %), while figure 1c illustrates the temperature absolute error (expressed

30   in K). The figure shows the noise error profiles estimated based on the application of the auto-

31   covariance method (described in detail in sub-section 4.1). More specifically, noise error assessments

32   have been performed considering two options for temporal and vertical resolution: a higher resolution

Atmospheric
Chemistry
and Physics
Discussions

Open Access

EGU

1   configuration, with a time resolution of 10 s and a vertical resolution of 90 m and 30 m for water vapour

2   mixing ratio and temperature, respectively (this is the selection considered for the turbulence

3   measurements); and a lower resolution configuration, with a time resolution of 150 m and a vertical

4   resolution of 5 min, which is the selection considered for the data set generated and uploaded to the

5   HOPE archive (primarily used for verification purposes, process studies and data assimilation). For the

6   first selection, the statistical error affecting water vapour mixing ratio measurements is smaller than 0.6

7   g kg^{-1} (or 50 %) up to 1.4 km, while the statistical error affecting temperature measurements is smaller

8   than 1 K up to 1.8 km. For the second selection, the statistical error affecting water vapour mixing ratio

9   measurements is smaller than 0.1 g kg^{-1} (or 15 %) up to 1.8 km, while the statistical error

10   affecting temperature measurements is smaller than 0,8 K up to 3 km. The above listed performances of

11   *BASIL* in terms of water vapour mixing ratio measurements result to be comparable with those reported

12   for the ARM Raman lidar (Wulfmeyer *et al.*, 2010, also 0.6 g kg^{-1} at 1.4 km), considering the same time

13   and vertical resolution. Same is true for the above listed performances of *BASIL* in terms of temperature

14   measurements, which indicate statistical uncertainties with values similar to those reported for the ARM

15   Raman lidar (Newsom *et al.*, 2013). The above quantified errors are used to derive - by means of error

16   propagation - the noise error profiles of the higher-order moments. An overview of these equations is

17   given in Wulfmeyer *et al.*, (2016).

18   In practice, water vapour mixing ratio and temperature profiles can be derived with different vertical

19   and temporal resolutions depending on the considered application. Vertical and temporal resolutions can

20   be traded-off with measurement precision, with random error affecting water vapour mixing ratio and

21   temperature measurements being inversely proportional to the square root of both vertical and temporal

22   resolution. Consequently, the consideration of the high temporal and vertical resolutions (10 sec, 30-90

23   m, respectively) needed for the characterization of turbulence processes translates into a lower

24   measurement precision (and consequently a larger statistical error). As a result of this, the

25   corresponding statistical error affecting daytime water vapour mixing ratio and temperature

26   measurements is smaller than 100 % and 1 K, respectively, up to 2 km (figure 1), these performances

27   being well suited for lidar measurements finalized to the characterization of turbulent variables.

28   Figure 1 also includes the error profiles obtained with the application of Poisson statistics to signal

29   photon counts. Signal photon counts are directly measured by the photon counting unit; "virtual" counts

30   can also be obtained from the signals measured by the analog module (Newsom *et al.*, 2009). In order to

31   get an estimate of the error affecting water vapour mixing ratio and temperature measurements through

32   Poisson statistics, it is necessary to first apply Poisson statistics to the photon counts of the individual

33   lidar signals contributing to the measurements and then, through error propagation, compute the overall

Atmospheric
Chemistry
and Physics
Discussions

1   error affecting the measured atmospheric variables. The error propagation expression is different for

2   water vapour mixing ratio and temperature measurements as different are the analytical expressions

3   relating the individual signals to the two measured parameters. For water vapour mixing ratio

4   measurements the application of error propagation yields the expression (Di Girolamo *et al.*, 2009a):

5
$$\frac{\Delta x_{H_2O}(z)}{x_{H_2O}(z)} = \sqrt{\frac{P_{H_2O}(z) + bk_{H_2O}}{P_{H_2O}^2(z)} + \frac{P_{N_2}(z) + bk_{N_2}}{P_{N_2}^2(z)}} \qquad (3)$$

6   where the terms bk_{H_2O} and bk_{N_2} represent the sky background signal (primarily associated with solar

7   irradiance) collected in the water vapour and molecular nitrogen channels, respectively. Expression (3)

8   provides the relative statistical error (in percent if multiplied for 100), while the absolute statistical error

9   can be obtained by multiplying expression (3) for $x_{H_2O}(z)$. The mean photon number for the 10 sec

10   water vapour and molecular nitrogen vibrational Raman signals, $P_{H_2O}(z)$ and $P_{N_2}(z)$, displayed in

11   figure 2, are found to vary featuring a maximum around 800 m of approx. 1500 and 12000 counts,

12   respectively, and progressively decreasing down to 0 and approx. 20 counts, respectively, around 10 km

13   (after background subtraction). Here the mean photon number is intended as the average of all 10 sec

14   signal profiles collected over the period 11:30-13:30 UT on 20 April 2013. Figure 2 also shows the

15   mean photon number for the 10 sec 354.7 nm elastic signal, $P_{354.7}(z)$, which has a maximum of approx.

16   2200 counts around 800 m and progressively decreases down to 2 counts around 10 km.

17   For temperature measurements the application of error propagation yields the expression (Behrendt *et*

18   *al.*, 2002, 2015, Di Girolamo *et al.*, 2006, 2009a):

19
$$\Delta T(z) = \frac{\partial T(z)}{\partial R} R(z) \sqrt{\frac{P_{LoJ}(z) + bk_{LoJ}}{P_{LoJ}^2(z)} + \frac{P_{HiJ}(z) + bk_{HiJ}}{P_{HiJ}^2(z)}} \qquad (4)$$

20   where the terms bk_{LoJ} and bk_{HiJ} represent the sky background signal collected in the low- and high-J

21   rotational Raman channels, respectively. The quantity $\partial T(z)/\partial R$ can be estimated based on the

22   application of the calibration procedure mentioned above. The mean photon number for the 10 sec low

23   and high quantum number rotational Raman signals, $P_{LoJ}(z)$ and $P_{HiJ}(z)$, also displayed in figure 2, is

24   found to vary featuring a maximum of approx. 4500 and 3500 counts, respectively, at 800 m, and

25   progressively decreasing down to 8 and 4 counts respectively, around 10 km. Figure 2 also shows the

26   temperature sensitivity of RRL measurement technique, i.e. the quantity $\partial R(z)/\partial T$, which is found to

27   vary between 0,06 K^{-1} at surface level to approx. 0,03 K^{-1} at 10 km, and the power ratio of high-to-low

28   quantum number rotational Raman signals, $R(z)$, which is found to vary between approx. 0,8 at surface

9

Atmospheric
Chemistry
and Physics
Discussions

1   level to approx. 0,3 at 10 km. The large values of the measurement sensitivity ($\partial R(z)/\partial T$) contribute to

2   the small random errors affecting the reported temperature measurements.

3   The terms bk_{H_2O} and bk_{N_2} in expression (3) and the terms bk_{LoJ} and bk_{HiJ} in expression (4) can be

4   determined considering the photon-counting signals at very high heights, this portion of the signals

5   being characterized by negligible contribution from laser backscatter photons and being typically

6   attributable to sky background radiation and intrinsic detector noise, the former being much larger than

7   the latter, especially for daytime operation. For the reported measurements, values of bk_{H_2O} and

8   bk_{N_2} are found to be approx. 11000 and 8000 counts, respectively, while values of bk_{LoJ} and bk_{HiJ} are

9   found to be approx. 200 and 1000 counts, respectively.

10   It is to be noticed that the auto-covariance analysis specifies the total statistical noise, while Poisson

11   statistics accounts only for its shot noise contribution, i.e. the contribution associated with the discrete

12   nature of the photons sampled by photon counting devices. Consequently, the application of Poisson

13   statistics to signal photon counts leads to an underestimation of the total statistical noise (Wulfmeyer *et*

14   *al.*, 2010, Behrendt *et al.*, 2015). Figure 1 reveals that noise error estimates obtained through the

15   application of Poisson statistics are in good agreement with estimates obtained through the auto-

16   covariance approach. Specifically, Poisson statistics accounts for approximately 75 % of the total

17   statistical noise affecting the measurement of water vapour mixing ratio and temperature. In more detail,

18   Poisson statistics accounts for 60 to 80 % of the total statistical noise affecting water vapour mixing

19   measurements, with a mean value of 74.5 %, while it accounts for 60 to 90 % of the total statistical

20   noise affecting temperature measurements, with a mean value of 78.0 %. This confirms that photon shot

21   noise represents the main contribution to the total statistical noise, but other statistical error sources,

22   usually very small, may also contribute.

23   As a result of the above described upgrades, *BASIL* performances in terms of the atmospheric variables

24   of interest for the purposes of this paper, extrapolated at higher hights based on the application of

25   Poisson statistics, are as follows. For water vapour mixing ratio measurements, the typical daytime

26   statistical error (precision) is smaller than 20 % up 3 km and smaller than 100 % up 4.5 km, while the

27   typical nighttime statistical error is smaller than 2 % up 3 km and smaller than 20 % up 9 km, based on

28   an integration time of 5 min and a vertical resolution of 150 m. The statistical error

29   affecting temperature measurements for daytime operation is typically smaller than 0.5 K up to 3 km

30   (figure 1) and smaller than 1.5 K up to 4.5 km, while for night-time operation is typically smaller

31   than 0.4 K up to 3 km (figure 1) and smaller than 1 K up to 6.5 km. These error values are consistent

Atmospheric
Chemistry
and Physics
Discussions

1   with the performances of the ARM water vapour Raman lidar (Wulfmeyer *et al.*, 2010; Turner *et al.*,

2   2014a).

3

4   **2.3 Systematic errors**

5   **2.3.1 Time independent systematic errors**

6   In addition to the statistical error, a small systematic error (bias) may affect both water vapour and

7   temperature measurements. For example, for water vapour measurements, besides a bias (not exceed

8   5 %) associated with the estimate of the calibration coefficient (resulting from radiosonde biases,

9   different air masses being sensed by the radiosonde and the lidar), an additional very small bias

10   (< 1 %) may be associated with the use of narrowband filters and, consequently, the accurate estimate of

11   the height-dependent correction factor accounting for the temperature dependence of the H_2O and N_2

12   Raman scattering signals selected by these filters, while a 1 % systematic uncertainty may be associated

13   with the determination of the differential transmission term (Whiteman, 2003). For temperature

14   measurements, besides a small bias associated with the estimate of the calibration coefficient, an

15   additional small bias (< 0.2 K) is associated with the assumption of the calibration function (1) to be

16   valid for the selected portions of the rotational Raman spectrum. It is to be pointed out that, as the above

17   mentioned systematic error sources are time independent (see Whiteman, 2003, for water vapour

18   measurements and section 4.2.2 of this paper for temperature measurements), biases can be

19   substantially removed from water vapour and temperature time-series measurements based on the use of

20   suitable spectral filters before calculating their fluctuations; consequently, time-independent systematic

21   errors have a marginal influence on the accuracy of turbulence profiles, especially for a high accuracy

22   system as ours (see equations A1-A8 in Wulfmeyer *et al*., 2016).

23

24   **2.3.2 Elastic signal leakage in the rotational Raman signals and approach for its removal**

25   Specific check and sensitivity studies have been performed in order to verify the presence and

26   amplitude of elastic signal leakages in the rotational Raman signals and their potential effect on

27   temperature measurements. In this respect it is to be pointed out that in the present system set-up the

28   low- and high-quantum number rotational Raman signals, $P_{LoJ}(z)$ and $P_{HiJ}(z)$, are collected at 354.3

29   and 352.9 nm, respectively, these wavelengths being very close to the laser emission at 354.7 nm.

30   Consequently, particular care has to be paid in the definition of the spectral specifications of the

31   interference filters used for the selection of $P_{LoJ}(z)$ and $P_{HiJ}(z)$, especially for what concerns their

Atmospheric
Chemistry
and Physics
Discussions

1   blocking at 354.7 nm. This is particularly true for the Lo-J filter, having a central wavelength just 0.4

2   nm off the excitation wavelength, while it is less for the Hi-J filter, as its central wavelength is 1.8 nm

3   off the excitation wavelength. The interference filters used in the present system set-up are

4   characterized by a nominal blocking at 354.7 nm of 10^{-6}-10^{-7}. However, based on measurements carried

5   out in the presence of clouds, we collected experimental evidence that the effective blocking of our Lo-J

6   filter is not better than 10^{-5}. For this motivation, in previous field deployments (among others, the

7   Convective and Orographically-induced Precipitation Study - COPS, Wulfmeyer *et al.*, 2008; Behrendt

8   *et al.*, 2011), a second narrow-band interference filter was put in cascade to the Lo-J filter, this second

9   filter having the same center wavelength and pass-band of the Lo-J filter (this latter being 0.2 nm full

10   width at half maximum), but having a nominal blocking at 354.7 nm of 10^{-3}. The combination of two

11   filters had been successfully applied before at 532 nm, obtaining undisturbed measurements even in

12   clouds (Behrendt and Reichardt, 2000). Just recently, the possibility to achieve sufficient blocking at

13   354.7 nm with only one filter could also be demonstrated based on recent advances achieved in multi-

14   cavity interference filter technology (Hammann *et al.*, 2015b). The ultimate goal of using two cascading

15   interference filters was to obtain an overall blocking at 354.7 nm of 10^{-8} or better. However, because of

16   the very narrow pass-band of the two cascading filters, a perfect superimposition of their transmission

17   curves was found difficult to achieve. In this respect it is to be specified that a partial superimposition of

18   the transmission curves of the two filters may determine an even narrower pass-band, ultimately

19   compromising the filters' capability to select the rotational lines necessary for the temperature

20   measurements. Additionally, also when a perfect superimposition of the two cascading filters'

21   transmission curves is achieved, the overall center wavelength transmission is significantly reduced (not

22   exceeding 15 %, with the transmission of the Lo-J filter being 30 % and the transmission of the second

23   cascading filter being 50 %); thus, the introduction of the second cascading filter determines an overall

24   reduction of $P_{LoJ}(z)$ by 50 % and a consequent reduction in measurement precision.

25   In order to avoid these drawbacks, in recent field deployments the second cascading filter was remove

26   from the Lo-J channel, fully aware that this would have determined an overall lower blocking at 354.7

27   nm for the Lo-J interference filter and, consequently, a possible leakage of the 354.7 nm elastic lidar

28   signal into the Lo-J rotational Raman signal, but also fully aware of the different research efforts, and

29   corresponding literature papers, dedicated to the definition of approaches to identify and remove elastic

30   signal leakages from the rotational Raman signals (Behrendt *et al.*, 2002; Su *et al.*, 2013). These authors

31   demonstrated that elastic signal leakage into the Lo-J rotational Raman signals can be completely

32   removed if simultaneous and co-located measurements of the elastic signal are available. Behrendt *et al.*

33   (2002) tested their approach on a rotational Raman lidar operating at 532 nm, while Su *et al.* (2013)

Atmospheric
Chemistry
and Physics
Discussions

1   applied their approach to a rotational Raman lidar operating at 354.7 nm. At 354.7 nm, the approach

2   considers the expression:

3
$$P_{LoJ}(z) = P_{LoJ}^{leak}(z) - k\,T_F\,P_{354.7}(z) \qquad (5)$$

4   with $P_{LoJ}^{leak}(z)$ being the leaked Lo-J rotational Raman lidar signal, $P_{LoJ}(z)$ being the effective Lo-J

5   rotational Raman lidar signal used for the derivation of temperature profiles, $P_{354.7}(z)$ being the 354.7

6   nm elastic lidar signal, T_F being the transmission of neutral density filters (used to attenuate the elastic

7   signals and avoid signal induced noise effects associated with the low range echoes), and k being the

8   leakage factor. Expression (5) specifies that, if the leakage factor is known, the effective Lo-J rotational

9   Raman signal can be determined from leaked Lo-J rotational Raman signal by simply subtracting the

10 354.7 nm elastic lidar signal from the latter.

11 In this respect, it is to be specified that the simultaneity and co-location of the measured Lo-J and 354.7

12 lidar signals is in our case quite a strict requirement, as in fact the signals necessary for the present

13 turbulence studies are acquired with high vertical and temporal resolution. In our system, the

14 simultaneity is guaranteed by the use of two distinct acquisition channels, with a common triggering,

15 included in a single sampling unit. The co-location of the measurements, i.e. the sounding of the same

16 atmospheric air column, is guaranteed by the use of the same large-aperture telescope for the collection

17 of the two signals and the proximity of the two detection channels within the optical layout of system.

18 In this direction, it is also to be specified that the elastic and rotational Raman scattering are stimulated

19 with the same laser wavelength (354.7 nm) and consequently the radiated air column is the same for the

20 two measurement channels.

21 An accurate estimate of the leakage factor k is of paramount importance to remove, or at least minimize,

22 potential systematic errors associated with any residual elastic signal leakage in the rotational Raman

23 signals. For this purpose, a modified version of the approach defined by Behrendt *et al*. (2002) was

24 applied. The approach is based on the selection of a measurement period with clouds, the calculation of

25 $P_{LoJ}(z)$ for different values of k and the selection of the value of k leading to temperature values inside

26 the cloud best fitting the temperature values from a near-by radiosonde.

27 For this purpose, we selected a 9 min time interval (13:38-13:46 UTC), shortly after the 2-h time period

28 considered for the turbulence analysis (11:30-13:30 UTC); as a result of this selection, the value of k

29 determined for this time interval can be effectively used to correct the data in the time interval

30 considered in the turbulence analysis. The 9 min time interval is characterized by the presence of high-

31 level clouds (cirrus clouds) extending between 7.9 and 9.8 km, which are not optically thick, with all

Atmospheric
Chemistry
and Physics
Discussions

1   measured lidar signals extending above the cloud top. This characteristic makes the selected time

2   interval particularly suited for the estimate of k. A 9 min time interval was considered in order to

3   achieve a sufficiently high signal statistics and, consequently, a lower uncertainty in the determination

4   of the correct value of k based on the above mentioned best fit procedure. Figure 3 shows the vertical

5   profiles of $P_{LoJ}^{leak}(z)$, $P_{HiJ}(z)$ and $T_F\,P_{354.7}(z)$ averaged over the 9 min interval. To better illustrate the

6   proposed approach, in figure 3 we focused our attention to the vertical interval 6-10 km. The elastic

7   signal $P_{354.7}(z)$ reveals the presence of several layers associated with cirrus clouds between 7.9 and 9.8

8   km, with a peak at 9.3 km. The figure clearly highlights the elastic signal leakage into $P_{LoJ}^{leak}(z)$ in the

9   height region inside the cloud, while no evidence of elastic signal leakage is present in $P_{HiJ}(z)$ in this

10   same height region. To apply the best fit procedure the radiosonde launched at 13:00 UTC from the

11   near-by launching station in Hambach (approx. 4 km E-SE) was considered. Considering an ascent

12   speed of 3.5 m s^{-1}, which is the average speed experienced by the present radiosonde in the height

13   interval from surface up to 10 km, the radiosonde is expected to cover the 8-10 km height region in the

14   time interval 13:38-13:46 UTC, which is exactly the time interval considered for the application of our

15   approach. The value of k leading to temperature values inside the cloud best fitting the radiosonde

16   temperature values was found to be 0.91. The best fit procedure considers all data points (approx. 70

17   points) within the height range where the cirrus cloud is located (7.9 and 9.8 km). This computation was

18   repeated at different times during the cirrus clouds appearance period (12:22-18:52 UTC), also

19   considering the data from the additional radiosondes available in this period (i.e. at 15:00 and 17:00

20   UTC). Results reveal that k has a constant value of 0.91, with very limited dispersion (0.01) around this

21   value, i.e. $k\pm\Delta k=0.91\pm0.01$ (Nocera, 2016). This result demonstrates that laser frequency or filter's

22   position fluctuations, potentially generable by thermal drifts inside the laser cavity or the filter's housing,

23   respectively, have negligible effects on k.

24   It is to be pointed out that leakage correction increases the statistical uncertainty affecting the

25   temperature measurement as a result of the subtraction of $P_{354.7}(z)$, which is affected by statistical noise,

26   from $P_{LoJ}^{leak}(z)$, also affected by statistical noise, the two statistical noises being uncorrelated.

27   Additionally, the correction factor k is determined with a certain degree of uncertainty (small, but not

28   negligible), which may lead to a residual systematic error (bias) affecting temperature measurements

29   after the application of the leakage correction approach. The systematic error associated with this

30   residual leakage may be estimated through error propagation, considering the expression for $T(z)$

31   including leakage correction:

Atmospheric
Chemistry
and Physics
Discussions

1

$$T(z) = \frac{\alpha}{\ln\left[\dfrac{P_{HiJ}(z)}{P_{LoJ}^{leak}(z) - k\,T_F\,P_{354.7}(z)}\right] - \beta}$$

(6)

2   with T_F being the overall transmission ($\sim 10^{-3}$) of the two neutral density filters located in front of the

3   354.7 nm interference filter. Consequently, the systematic error affecting each temperature profile

4   associated with the uncertainty affecting k reads:

5

$$\Delta T_{leak}(z) = -\frac{T^2(z)}{\alpha}\frac{k\,T_F\,P_{354.7}(z)}{P_{LoJ}^{leak}(z) - k\,T_F\,P_{354.7}(z)}\frac{\Delta k}{k} \cong -\frac{T^2(z)}{\alpha}\frac{k\,T_F\,P_{354.7}(z)}{P_{LoJ}^{leak}(z)}\frac{\Delta k}{k} = -\frac{T^2(z)}{\alpha}\frac{T_F\,P_{354.7}(z)}{P_{LoJ}^{leak}(z)}\Delta k$$

(7)

6   with $\varDelta k$ being the uncertainty affecting the estimate of k. The leakage signal is $k\,T_F\,P_{354.7}(z)$, which

7   corresponds to about 22 % of $P_{LoJ}^{leak}(z)$ around the ABL top. Thus, the remaining error affecting

8   temperature measurements becomes a fluctuating error, which is dependent on atmospheric properties,

9   mainly on aerosol backscatter contribution to $P_{354.7}(z)$. This effect has to be properly taken into account

10   in the determination of turbulence profiles, as in fact fluctuations in aerosol particle backscatter,

11   especially in the upper portion of the CBL, may produce a time-dependent residual systematic error,

12   which would propagate into the temperature fluctuations. Because of this, the quantity

13     $P_{LoJ}(z) = P_{LoJ}^{leak}(z) - k\,T_F\,P_{354.7}(z)$ has to be properly assessed in expression (6) for each 10 s temperature

14   profile.

15   Considering an uncertainty of 0.01 on the estimate of k, a value of T=280 K, a value of α=1200 K

16   (which is the one resulting from the application of the calibration procedure), the systematic error

17     $\varDelta T_{leak}(z)$ associated with residual leakage in the upper portion of the CBL results to be equal to 0.16 K.

18   An additional overall, spurious term $\overline{\left(T'_{ov,leak}(z)\right)^2}$ has to be considered in the temperature variance, which

19   is associated with the residual systematic error affecting temperature measurements after the application

20   of the leakage correction approach. This additional contribution is given by:

21

$$\overline{\left(T'_{ov,leak}(z)\right)^2} \approx \overline{\Delta T_{leak}^{'\,2}} + 2\overline{T'_{tr}(t)\,\Delta T'_{leak}(t)} < \overline{\Delta T_{leak}^{'\,2}} + 2\sqrt{\overline{\Delta T_{leak}^{'\,2}}}\sqrt{\overline{T_{tr}^{'\,2}}}$$

(8)

22   where the first term in the contribution to the "leakage variance" due to additional fluctuations caused

23   by insufficient leakage correction and the second term is due to the correlation of the atmospheric

24   temperature fluctuations within the not perfectly corrected leakage. We find that:

Atmospheric
Chemistry
and Physics
Discussions

$$\overline{\Delta T'_{leak}}^2 \cong \left[\frac{T^2}{\alpha}\right]^2 \frac{(k\,T_F)^2\overline{\left(P_{354.7}(t)-\overline{P}_{354.7}\right)^2}}{\left(\overline{P}^{leak}_{LoJ}-k\,T_F\,\overline{P}_{354.7}\right)^2}\left(\frac{\Delta k}{k}\right)^2 = \left[\frac{T^2}{\alpha}\right]^2 \frac{\left(k\,T_F\,\overline{P}_{354.7}\right)^2}{\left(\overline{P}^{leak}_{LoJ}-k\,T_F\,\overline{P}_{354.7}\right)^2}\left(\frac{\Delta k}{k}\right)^2 \frac{\overline{\left(P_{354.7}(t)-\overline{P}_{354.7}\right)^2}}{\overline{P}_{354.7}^{\,2}}$$

1

$$= \left(\Delta T_{leak}\right)^2 \frac{\overline{\left(P_{354.7}(t)-\overline{P}_{354.7}\right)^2}}{\overline{P}_{354.7}^{\,2}} = \left(\Delta T_{leak}\right)^2 \frac{\mathrm{var}\left(\overline{P}_{354.7}\right)}{\overline{P}_{354.7}^{\,2}} \approx (0.18\mathrm{K})^2 \frac{1.7\cdot10^4}{500^2} = 2.2\cdot10^{-3}\,\mathrm{K}^2 \qquad (9)$$

2 where we took the relative variance of the backscatter signal from our data at the ABL top. Here, the

3 variance is maximum so that we reach an upper limit of the spurious temperature variance of

4 $2.2\cdot10^{-3}\,\mathrm{K}^2$ which can be neglected with respect to the atmospheric temperature variance (see section

5 4.3). For the correlation term, however, we get

6 $$2\overline{T'_{tr}(t)\,\Delta T'_{leak}(t)} < 2\sqrt{\overline{\Delta T'_{leak}}^2}\sqrt{\overline{T'_{tr}}^2} \approx 2\cdot0.048\mathrm{K}\cdot0.64\mathrm{K} = 0.06\mathrm{K}^2 \qquad (10)$$

7 where we took the maximum of the atmospheric temperature variance at the ABL top. This error is still

8 considerably smaller than our estimate of the atmospheric temperature variance at the peak in the

9 entrainment layer so that the structures in the higher-order moments are significant.

10 Based on the above considerations, we have to be aware that, besides a random error, represented in

11 figure 6b with the error bar, an additional systematic error (with a maximum amplitude of 0.16 K)

12 resulting from residual elastic signal leakage in the rotational Raman signals has to be considered. This

13 is also true when considering the noise error estimated in figure 1c. The missed inclusion of this

14 systematic error both in figure 6b and figure 1c is due to the very small amplitude of this contribution;

15 additionally, random and systematic error sources have always to be treated separately and cannot be

16 just summed up. Additionally, the spurious temperature variance, even if small with respect to the

17 atmospheric temperature variance, it is always positive. So an iteration with different values for k can

18 also be used to verify the correctness of the above determined value of k, as in fact the correct value

19 minimizes the overall variance.

20 Based on the above mentioned approach, before proceeding with the turbulence analysis, we corrected

21 all 10 sec Lo-J signals for the systematic effect associated with elastic signal leakage. However, in order

22 to overcome the residual systematic uncertainty associated with this correction, a future upgrade of

23 *BASIL* is planned with the introduction of a new Lo-J filter, with high blocking at 354.7 nm and high

24 center wavelength transmission, to be developed benefiting from the recent advances in multi-cavity

25 interference filter technology.

26

27

Atmospheric
Chemistry
and Physics
Discussions

1   3 Time-height cross-sections of water vapour mixing ratio and temperature

2   3.1 Case study and weather conditions

3   In this paper we illustrate measurements carried out in the framework of the HD(CP)2 Observational

4   Prototype Experiment (HOPE). HOPE, embedded in the project High-Definition Clouds and

5   Precipitation for advancing Climate Prediction (HD(CP)2) of the German Research Ministry, was

6   specifically designed to provide a dataset for the evaluation of the German non-hydrostatic General

7   Circulation Model ICON at the scale of the model simulations. It took place in Western Germany in the

8   time period April-May 2013. For the purposes of HOPE, *BASIL* was deployed in the Supersite JOYCE,

9   located within the Jülich Research Center (Central Germany, Lat.: 50°54' N; Long.: 6°24' E, Elev. 105

10   m). The system operated between 25 March and 31 May 2013, collecting more than 430 hours of

11   measurements distributed over 44 days and 18 IOPs. Quick-looks of these dataset are present on the

12   HOPE Website (https://code.zmaw.de/projects/hdcp2-obs/), while water vapour and particle backscatter

13   data can be downloaded from the HD(CP)2 database.

14   In the selection of the case study considered in this paper, attention was paid on identifying weather

15   conditions characterized by the presence of a well-mixed and quasi-stationary CBL. Consequently, in

16   those cases when measurements of the complete CBL cycle are available, i.e. from the onset to its

17   progressive built up and final decay, attention has been focused only on those time segments

18   characterized by a stable or almost stable CBL height, which corresponds to the period of its maximum

19   development. Typically time segments with a duration of 1-2 hours are considered as in fact for longer

20   periods the CBL can no longer be considered as being quasi-stationary, while the consideration of

21   shorter periods would reduce the number of sampled thermals and thus increase the sampling errors.

22   The synoptic condition on 20 April 2013 was characterized by the presence of a high pressure system

23   located over Great Britain, with effects extending over Central-Northern Germany, and a low pressure

24   system located over Central Italy (see also Muppa *et al.*, 2016). The forecast for the HOPE region

25   indicated some thin convective clouds from 8 to 10 UTC and clear sky starting from 10 UTC, with

26   cirrus clouds startind from 15 UTC. This was considered as a day with suitable atmospheric conditions

27   for an Intensive Observation Period (IOP), specifically IOP 5, dedicated to radiometer tomography.

28   This IOP turned out to be also a good case study for the purpose of studying CBL development under

29   clear-sky or almost-clear sky conditions. Indeed, the almost undisturbed solar irradiance resulted in the

30   development of a well-mixed CBL which was not affected by clouds.

31

32

1 **3.2 Water vapour mixing ratio, temperature, and backscatter fields**

2 In order to select an appropriate time interval for the application of the turbulence analysis, we

3 considered the measurements of the different energy balance components as provided by the surface

4 energy balance station in Hambach (not illustrated here). The maximum net radiation was found to

5 occur around 12:00 UTC (520 Wm^{-2}), with a very limited variability (<40 Wm^{-2}) within the time

6 interval 11:30-13:30 UTC. This is the time interval that we selected for the turbulence analysis.

7 In order to achieve a sufficiently high signal-to-noise error (SNR) and consequently an acceptably low

8 noise error level, a running average over 3 points was considered for the water vapour mixing ratio data,

9 which translates into a reduced vertical resolution of 90 m, while no average was applied to the

10 temperature data, keeping the original vertical resolution of 30 m.

11 Figure 4 illustrates the time-height plot of the particle backscatter coefficient at 1064 nm, β_{par}, between

12 11:30 and 13:30 UTC on 20 April 2014. The figure reveals the presence of a significant aerosol loading

13 within the boundary layer (with values of β_{par} in excess of 1×10^{-6} m^{-1} sr^{-1}), tracing the presence of a

14 well-mixed and quasi-stationary CBL at this time of the day, extending up to a height of approximately

15 1300 m. The figure also reveals the presence of alternating updrafts and downdrafts. β_{par} was

16 determined based on the application of a Klett-modified approach (Di Girolamo *et al.*, 1995, 1999). The

17 identification of the CBL height and the monitoring of its variability is made possible by exploiting

18 aerosols' property to act as atmospheric tracers. The mean CBL height, z_i, is an important scaling

19 variable for turbulence profiles. The evolution of the instantaneous CBL height z'_i (black dots in figure

20 4) was determined through the application of a conventional approach based on the detection of the

21 strongest gradient of the aerosol backscatter signal (see, among others, Pal *et al.*, 2010; Summa *et al.*,

22 2013). Within the considered time interval z'_i is found to be characterized by a limited variability, with a

23 mean value z_i of 1290 m a.g.l and a standard deviation of 77 m. The minimum and maximum values of

24 z'_i during the observation period are 1140 and 1440 m a.g.l., respectively. This result is in very good

25 agreement with the simultaneous measurements performed by the University of Hohenheim Differential

26 Absorption Lidar (UHOH-DIAL) (Wagner *et al.*, 2013; Späth *et al.* 2016), deployed in Hambach,

27 approx. 4 km E-SE, with a mean value of 1295 m and a standard deviation of 86 m (Muppa *et al.*,

28 2016). z_i is used in the remaining part of the paper to determine the normalized height scale z/z_i. Particle

29 backscatter coefficient data can also be used to identify the presence of aerosol layers and/or clouds

30 within and above the CBL, with an effective demonstrated capability to detect cloud bases and tops (the

31 latter in the case of cloud optical thickness typically smaller than 2, Di Girolamo *et al.*, 2009b).

Atmospheric
Chemistry
and Physics
Discussions

1   Figure 5 illustrates the time-height cross section of water vapour mixing ratio (figure 5a) and

2   temperature (figure 5b) for the same time interval considered in figure 4. Figures 5a and 5b clearly

3   highlights the large variability of water vapour mixing ratio and temperature within the CBL associated

4   with the presence of alternating updrafts and downdrafts. The largest variability of both water vapour

5   mixing ratio and temperature is observed in the interfacial layer, as a result of the penetration of the

6   warm humid air rising from the ground and the entrainment of cool dry air from the free troposphere.

7   Figure 5b also reveals the presence of decreasing temperatures within the CBL up to a minimum around

8   1200-1300 m and an appreciable temperature inversion (approx. 1 K) above.

9   Figure 6 illustrates the mean profile for water vapour mixing ratio (figure 6a) and temperature (figure

10   6b) as measured by *BASIL* over the same time interval considered in figure 4 (11:30-13:30 UTC on 20

11   April 2013), together with the corresponding profiles measured by the radiosonde launched at 13:00

12   UTC from the nearby site of Hambach. The water vapour mixing ratio profiles from *BASIL* and the

13   radiosonde are found to agree within 0.2 g kg^{-1} within the mixed layer. A larger deviation is found in the

14   interfacial layer (0.5 g kg^{-1}). However, this is not surprising when considering that the Raman lidar data

15   are averaged over a 2 h period (11:30-13:30 UTC), while the radiosonde reaches the CBL top few

16   minutes after launch. Besides the different time interval considered for *BASIL* and the radiosonde, the

17   two sensors are also sounding different air masses as a result of the 4 km distance between the lidar site

18   and the radiosonde launching station and the horizontal drift of the sonde during its ascent caused by the

19   wind and the consequent deviation of its atmospheric path from the vertical. In presence of intense

20   convective activity, deviations from the sounding data are also possible for radiosondes launched from

21   the lidar site: in this case humid air updrafts and dry air downdraft may have sizes of few kilometres and

22   consequently the radiosonde data can capture different features during its ascent within the CBL with

23   respect to the lidar. This property makes lidar systems much more suitable for studying turbulence

24   statistics than in-situ sounding systems as in fact with lidars statistics is indeed measured in a vertical

25   column. Similar considerations apply for the comparison between *BASIL* and the radiosonde in terms of

26   temperature profile (figure 6b). In this case, the deviation between the two sensors is ≅0.5 K throughout

27   the CBL, with *BASIL* being characterized by systematically smaller values than the radiosonde, while a

28   better agreement (deviation not exceeding 0.3 K) is observed in the free troposphere above the CBL top.

29   In this respect, it is to be noticed that the sequence of consecutive radiosondes launched during IOP 5

30   (at 09:00, 11:00, 13:00 UTC, not shown here) reveals the occurrance of vertical profiles characterized

31   by an almost constant potential temperature values within the mixed layer, as expected for a well-mixed

32   CBL, with potential temperature constant value progressively increasing with time. Considering that

33   Raman lidar data in figure 6 are averaged over a 2 h period (11:30-13:30 UTC) which is largely

Atmospheric
Chemistry
and Physics
Discussions

1   anticipating the radiosonde launch time (at 13:00 UTC), the systematically smaller temperature values

2   of *BASIL* with respect to the radiosonde within the CBL are easily justifiable.

3

4   **4 Turbulence analysis methodology and results**

5   **4.1 Methodology**

6   In CBL turbulence studies, the instantaneous value of a measured atmospheric variable, $x(z,t)$, at height

7   z, can be expressed as the sum of three terms: a slowly varying or even constant term, $\overline{x(z)}$, where the

8   over-bar represents the time average over the considered temporal interval for the turbulence analysis, a

9   fluctuation or perturbation term, $x'(z,t)$ and a system noise term, $\varepsilon(z,t)$, following the expression:

10   $$x(z,t) = \overline{x(z)} + x'(z,t) + \varepsilon(z,t) \qquad (11)$$

11   $\overline{x(z)}$ can be derived from applying a linear fit to the data over the time period when the turbulent

12   processes are studied (typically 60-120 min, 120 min in our case).

13   Here the fluctuation term $x'(z,t)$ represents the de-trended fluctuation term with zero mean. To de-trend

14   the data within a CBL in quasi-stationary state a linear fit is applied to the atmospheric variable time

15   series.

16   For any measured atmospheric variable, as atmospheric variance and the noise variance are uncorrelated,

17   total variance can be expressed as (Lenschow *et al*., 2000):

18   $$\overline{\left(x'_m(z)\right)^2} = \overline{\left(x'_a(z)\right)^2} + \overline{\left(x'_n(z)\right)^2} \qquad (12)$$

19   with $\overline{\left(x'_m(z)\right)^2}$ being the total measured variance, $\overline{\left(x'_a(z)\right)^2}$ being the atmospheric variance and

20   $\overline{\left(x'_n(z)\right)^2}$ being the noise variance.

21   Different procedures may be considered to separate atmospheric variance from noise variance in the

22   total measured variance. The auto-covariance method is probably the most effective and straightforward

23   among these procedures. This method is based on the consideration that atmospheric fluctuations are

24   correlated in time, while instrumental noise fluctuations are uncorrelated (Lenschow *et al*., 2000). This

25   approach allows to determine atmospheric variance based on the computation of the auto-covariance

26   function (ACF) for the considered atmospheric variable and then extrapolating this function to zero lag

27   based on the application of a power-law fit. As specified in Lenschow *et al*. (2000), the auto-covariance

1   function at zero lag represents the total measured variance and, consequently, the noise variance can be

2   determined as the difference between the auto-covariance function extrapolated to zero lag and its value

3   at zero leg.

4   An alternative approach is represented by the spectral method. In this case, the power spectrum of the

5   atmospheric variable fluctuations is computed and the constant white noise level close to the Nyquist

6   frequency is evaluated. Both the spectral method, based on the assumption that the system noise is

7   white, and the auto-covariance method allow to verify whether the major part of the turbulent

8   fluctuations is resolved through the measurements either by comparing the high-frequency component

9   of the spectrum with the theoretical decay in the inertial sub-range or by fitting the turbulent structure

10 function to the auto-covariance function. Thus, there is no reason to transfer the data in the spectral

11 domain for these applications and, because of that, the data analysis was kept in the time domain.

12 Furthermore, while both approaches were considered and tested on the water vapour and temperature

13 data considered in this paper, the auto-covariance technique (see figure 1) is to be preferred because of

14 its capability to directly determine system noise variance by means of the Fourier transformation of the

15 auto-covariance function, without introducing additional uncertainties (Wulfmeyer *et al*., 2010).

16 Preliminary pre-processing steps have to be applied to the data before both techniques can be applied. In

17 general, before any further processing, spikes must be detected and flagged, as they negatively affect

18 the calculation of turbulent variables (Senff *et al*., 1996). In fact, the presence of spikes in the time

19 series may have a significant impact on the computations of higher moments of the turbulent statistics.

20 Spikes in water vapour and temperature profiles are primarily resulting from non-linear effects

21 associated with the application of retrieval algorithms, these being likely to happen especially at low

22 signal-to-noise levels (Di Girolamo *et al*., 2008). Low signal-to-noise levels are typically found in day-

23 time Raman lidar water vapour and temperature measurements at heights above 3-5 km, this height

24 varying depending on the considered variable (being lower for water vapour and higher for temperature),

25 or in the presence of clouds as a result of the laser beam attenuation. For the application considered in

26 this paper, i.e. the characterization of turbulent processes within the CBL, the vertical range of interest

27 is up to 2000 m and within this range the signal-to-noise level of rotational and vibrational Raman

28 signals is typically large enough to refrain from applying the spike removal algorithm to the data.

29 Additionally, for the specific case study considered in this paper, clouds are completely missing within

30 the CBL, and consequently the application of the spike removal algorithm to the lidar data returns a

31 dataset with almost no data removed. However, there may be missing data or data gaps generated in the

32 adaptation of the time resolution; because of this, a spike detection algorithm (McNicholas and Turner,

Atmospheric
Chemistry
and Physics
Discussions

1 2014) is routinely applied to the data before either the auto-covariance method or the spectral method

2 are applied.

3

4.2 Turbulent fluctuations, corresponding auto-covariance functions and assessment of the noise

error

6 Figure 7 illustrates the time-height cross section of water vapour mixing ratio (figure 7a) and

7 temperature fluctuations (figure 7b) in the same time interval considered in figure 4. Positive and

8 negative humidity and temperature fluctuations are present within the CBL. In the interfacial layer, the

9 fluctuations become larger than below. More specifically, instantaneous water vapour fluctuations are

10 within $\pm$ 0.5 g kg^{-1} in the mixed layer and $\pm$ 1 g kg^{-1} in the interfacial layer, while instantaneous

11 temperature fluctuations are within $\pm$ 0.5 K in the mixed layer and $\pm$ 1 K in the interfacial layer. In the

12 free troposphere humidity and temperature fluctuations are almost completely missing and the observed

13 variability is primarily driven by instrumental noise.

14 Figure 8 shows the auto-covariance functions obtained from water vapour (figure 8a) and temperature

15 fluctuations (figure 8b) for the height levels between 400 and 1600 m a.g.l., i.e., 0.3 to 1.25 z_i, and for

16 lags from -200 to 200 s. As mentioned earlier, the difference between the peak at zero lag and the first

17 lag provides an estimate of the system noise variance. This is also described in figures 8a and 8b, where

18 the structure functions have been fitted to the auto-covariance functions for the height levels of 1230 m

19 and 1410 m to verify the feasibility and reliability of this approach. In the figure, this difference is

20 found to increase with height for both variables as a result of the increasing system statistical noise.

21 Values of the ACFs close to the zero lag provide an estimate of the atmospheric variance: larger values

22 for the ACFs found in the figure at 1230 and 1410 m indicate a larger atmospheric variance at these

23 heights, as a result of the large atmospheric variability within the interfacial layer.

24

4.3 Measurements of higher-order moments

26 Figure 9 illustrates the integral scale (IS) of water vapour mixing ratio (figure 9a) and temperature

27 fluctuations (figure 9b) computed for the same time interval considered in figure 4. The integral time

28 scale can be considered as an estimate of the mean size of the turbulent eddies involved in the boundary

29 layer mixing processes. The integral time scale of both water vapour mixing ratio and temperature

30 fluctuations is found to have large values (also exceeding 200 s) in the lower portion of the CBL up to

31 $\cong$ 750 m (i.e. z/z_i <0.6). Values of the integral scale for water vapour mixing ratio fluctuations in the

Atmospheric
Chemistry
and Physics
Discussions

Open Access

1   upper portion of the CBL (above 750 m) are in the range 70-125 s, with a peak value of 125 s at 1230 m

2   (i.e. z/z_i=0.95). These values are in agreement with those reported for water vapour by Wulfmeyer *et al.*

3   (2010, 70-130 s) and by Turner *et al.*, 2014a (120-140), as well as with the simultaneous nearby

4   measurements performed by the UHOH-DIAL, with values in the range 60-130 s (Muppa *et al.*, 2016).

5   Values of the integral scale for temperature fluctuations in the upper portion of the CBL are in the range

6   75-225 s, with a peak value of 225 s around the top of the CBL (at 1310 m). These values are in

7   agreement with those reported by Behrendt *et al.* (2015, 40-120 s) for the nearby site of Hambach, but a

8   different case study. Values of the integral scale throughout the CBL for both water vapour and

9   temperature fluctuations are much larger than the temporal resolution used for the measurements (10 s),

10 which demonstrates that the considered temporal resolution is high enough to characterize the major

11 part of turbulence inertial sub-range and consequently resolve the major part of the CBL turbulent

12 fluctuations.

13 Figure 10 shows the vertical profiles of atmospheric and total variance for water vapour mixing ratio

14 (panel a) and temperature (panel b), including noise errors. Water vapour mixing ratio variance is

15 almost zero up to $\cong$ 750 m (i.e. z/z_i=0.6), it keeps small (<0.05 g^2kg^{-2}) in the middle and upper portion

16 of the CBL (750 m <z< 1100 m, i.e. 0.6<z/z_i<0.85), and it sensitively increases in the interfacial layer

17 due to the entrainment effects. The maximum of the variance profile in the interfacial layer is 0.287

18 g^2kg^{-2} at 1260 m (i.e. z/z_i=0.98), with 0.051 g^2kg^{-2} and 0.034 g^2kg^{-2} being the sampling error and noise

19 error, respectively. The near-zero values in the lower portion of the CBL are typical and indicate weak

20 forcing from the surface. In the interfacial layer, the variance reaches a maximum as a result of the large

21 water vapour mixing ratio variability which is generated by the vertical exchange associated with the

22 strong updrafts and downdrafts (Wulfmeyer *et al.*, 2010; Turner *et al.* 2014a, Muppa *et al.*, 2016).

23 Variance values at the top of the CBL are in good agreement with those reported by Wulfmeyer

24 (1999a,b, 0.1–0.2 g^2kg^{-2}), Lenschow *et al.* (2000, 0.1–0.2 g^2kg^{-2}) and Kiemle *et al.* (1997, 0.3–0.45

25 g^2kg^{-2}), as well as with the simultaneous nearby measurements by the UHOH-DIAL, with a peak value

26 in the interfacial layer of 0.39 g^2m^{-6}, corresponding to 0.19 g^2kg^{-2}. The full width at half maximum of

27 the largest variability in the entrainment zone is 240 m, i.e. 0.19 z/z_i, in agreement with measurements

28 reported by Wulfmeyer *et al.* (2010, 0.16 z/z$_i$) and by Turner *et al.* (2014a, 0.15 z/z$_i$). Values of water

29 vapour mixing ratio variance decrease above the CBL top to approach zero around 1500 m.

30 For what concerns the temperature variance, this keeps smaller than 0.1 K^2 in the middle and upper

31 portion of the CBL up to 1150 (i.e. z/z_i<0.9). Larger values are observed in the interfacial layer, with a

32 maximum of 0.260 K^2 at 1310 m (i.e. z/z_i=1.02), with 0.051 K^2 and 0.035 K^2 for the sampling error and

33 noise error, respectively. Larger values of the temperature variance in the interfacial layer are the result

Atmospheric
Chemistry
and Physics
Discussions

Open Access

EGU

1   of the penetration of the warm humid air rising from the ground and the entrainment of cool dry air

2   from the free troposphere (Stull, 1988; Behrendt et al., 2015; Wulfmeyer et al., 2016). Temperature

3   variance decreases above the CBL top to approach zero around 1450 m. The full width at half

4   maximum of the largest variability in the entrainment zone is 240 m, i.e. z/z_i=0.2. Similar peak variance

5   values (0.40 K^2) at the top of the CBL were also observed by Behrendt et al. (2015) and Wulfmeyer et

6   al. (2016). It is to be noticed that both water vapour mixing ratio and temperature variance are

7   characterized by very small sampling and noise errors, which make the quality of the present turbulence

8   measurements very high and demonstrates how well the structures present in these profile can be

9   determined.

10   Figure 11 illustrates the vertical profiles of the third-order moment for water vapour mixing ratio (panel

11   a) and temperature (panel b). The third-order moment of a variable quantifies the degree of asymmetry

12   of its distribution, with positive values indicating a right-skewed distribution (with the mode smaller

13   than the mean) and negative values indicating a left-skewed distribution (with the mode larger than the

14   mean). Again, third-order moment estimates are characterized by very small errors, which testify the

15   high quality of the present measurements of this turbulent variable. In figure 11 values of the third order

16   moment of water vapour mixing ratio fluctuations are found to be close to zero between 400 and 900 m

17   (i.e. for 0.3 z_i < z < 0.7 z_i) and are negative between 900 and 1290 m (i.e. for 0.7 z_i < z < z_i), with a

18   negative peak value of -0.029±0.005 g^3kg^{-3} at 1140 m. A large positive peak is observed just above

19   CBL top, with a maximum of 0.156±0.009 g^3kg^{-3} at 1380 m (z=1.07 z_i).

20   Negative values for the water vapour mixing ratio third-order moment in the upper portion of the CBL

21   is the result of the sharp entrainment of dry air pockets into the boundary layer, which gradually mix

22   with the environmental air (Couvreux et al., 2005, 2007; Wulfmeyer et al., 2010; Turner et al., 2014a,

23   Wulfmeyer et al., 2016). Positive values for the water vapour mixing ratio third-order moment above

24   the top of the CBL are associated with narrow, but strong, convective plumes that penetrate up to this

25   height. The sign and shape of the third-order moment at the top of the boundary layer may also depend

26   on the humidity gradient above the CBL (Couvreux et al., 2007). The near-zero third-order moment

27   values in the mixed layer (z/z_i < 0.7) is to be attributed to a symmetric transport process of moisture

28   (Mahrt, 1991; Wulfmeyer et al., 2010).

29   For what concerns the temperature third-order moment, this shows values close to zero (<0.01 K^3) up to

30   1100 m (z/z_i < 0.85) and slightly positive values between 1100 and 1310 m (0.85 z_i < z < 1.02 z_i), with

31   a positive peak of 0.055 K^3 at 1220 m. Above 1250 m it becomes negative, with a negative peak of -

32   0.067±0.01 K^3 at 1400 m (z/z_i=1.1). The structure of this moment is basically inverted with respect to

Atmospheric
Chemistry
and Physics
Discussions

Open Access

1   water vapour (Behrendt *et al.*, 2015). This makes sense because the water vapour gradient is negative in

2   the entrainment zone, whereas the temperature inversion gradient is positive. The positive peak in the

3   interfacial layer is evidence of the predominant effect of narrow warm air downdrafts in the interfacial

4   layer, while the negative peak above the CBL top is the result of narrow cooler updrafts above the CBL

5   top associated with thermals from the surface. Figure 11b, besides temperature third-order moment, also

6   includes the vertical profile of the water vapour mixing ratio third-order moment to better compare the

7   shapes and locations of the peaks and zero crossing values for these two profiles. This allows to reveal

8   that the negative peak in the temperature third-order moment appears at the same height (within 20 m)

9   of the positive peak in the water vapour mixing ratio third-order moment, while the distance between

10 the zero crossing values for the two profiles is approx. 100 m.

11 Figure 12 illustrates the vertical profiles of the fourth-order moment for water vapour mixing ratio

12 (panel a) and temperature (panel b). The fourth-order moment of a variable gives an indication of the

13 steepness of its distribution and the width of its peak. Water vapour mixing ratio fourth-order moment is

14 almost zero up to $\cong$ 750 m (i.e. z/z_i=0.6), keeps smaller than 0.02 g^4kg^{-4} in the middle and upper portion

15 of the CBL (750 m <z< 1100 m, i.e. 0.6<z/z_i<0.85) and increases above 1100 m, reaching its maximum

16 of 0.28±0.13 g^4kg^{-4} around the top of the CBL (at 1350 m). It gets again close to zero above 1530 m.

17 Similarly, temperature fourth-order moment is almost zero (<0.05 K^4) up to 1100 m (i.e. z/z_i=0.85) and

18 has positive values above, reaching a positive peak of 0.24±0.10 K^4) around the top of the CBL (at 1370

19 m, i.e. z/z_i=1.06). It gets again smaller than 0.05 K^4 above 1500 m (i.e. z/z_i=1.15).

20 Besides the third- and fourth-order moments, also atmospheric skewness and kurtosis has been

21 determined for both water vapour mixing ratio and temperature fluctuations. Figure 13 illustrates the

22 vertical profiles of skewness (panel a) and kurtosis (panel b) for water vapour mixing ratio and

23 temperature. Values of water vapour mixing ratio skewness are in very good agreement with those

24 reported by Wulfmeyer *et al.*, 2010, with positive values (up to 1.5) in the lower portion of the CBL (up

25 to 800 m, i.e. z/z_i=0.65), with negative values (down to -1) in the middle and upper portion of the CBL

26 (800<z< 1290 m, i.e. 0.65<z/z_i<1.00) and positive values just above the PBL top (with a maximum of

27 approx. 5 at 1400 m, i.e. z/z_i=1.15). Values and vertical structure of water vapour mixing ratio skewness

28 are also in good agreement with the simultaneous and nearby measurements performed by the UHOH-

29 DIAL (Muppa *et al.*, 2016), with negative values (down to -1.16) in the middle and upper portion of the

30 CBL (0.35<z/z_i<1.00) and positive values just above the PBL top (with a maximum of approx. 1 at z/z_i

31 =1.05), as well as with the measurements reported by Turner *et al.* (2014), with negative values (down

32 to ~ -1) up to the CBL top, zero values around z_i and positive values just above the CBL top (with a

33 maximum of approx. 1 at z/z_i=1.1).

Atmospheric
Chemistry
and Physics
Discussions

1 Temperature skewness has a negative peak ($\sim$ -4) at 500 m, i.e. z/z_i =0.4, positive peaks ($\sim$ 4 and 8) at

2 890 and 1100 m (i.e. z/z_i =0.7 and z/z_i =0.85), respectively, and a negative peak ($\sim$ -7) at 1460 m, i.e. z/z_i

3 =1.13, in in good agreement with measurements reported by Behrendt *et al.* (2015, 40-120 s) for the

4 nearby site of Hambach, but a different case study.

5 Values of kurtosis in the entrainment zone (in the height interval 1160-1340 m) are in the range 2.35-

6 4.33, with a mean value of 3.15, for water vapour mixing ratio fluctuations, while they are in the range

7 2.59-4.11, with a mean value of 3.22, for temperature fluctuations. These values indicate normally

8 distributed (mesokurtic-Gaussian distribution) humidity and temperature fluctuations in the entrainment

9 zone (Wulfmeyer *et al.*, 2010; Turner *et al.* 2014a, Behrendt *et al.*, 2015, Muppa *et al.*, 2016).

10

11 **5 Summary**

12 This paper illustrates measurements performed by the Raman lidar system *BASIL* during a recent field

13 deployment which demonstrate the capability of this remote sensor to characterize turbulent processes

14 within the CBL. For the first time simultaneous and co-located daytime measurements of the vertical

15 profiles of higher-order moments of the turbulent fluctuations of water vapour and temperature carried

16 out by a single instrument are reported. Thus, this paper demonstrates that state-of-art lidar systems,

17 with both rotational and vibrational Raman measurement capability, allow for simultaneously

18 determining higher-order moments (as well as skewness and kurtosis) of the fluctuations of these two

19 fundamental turbulent variables. Results are based on the application of the auto-covariance analysis

20 introduced by Lenschow *et al.* (2000) to high-resolution water vapour mixing ratio (10 s, 90 m) and

21 temperature (10 s, 30 m) time series.

22 Measurements of water vapour turbulent fluctuations throughout the CBL by vibrational Raman lidar,

23 with estimates of up to the fourth-order moment, had been demonstrated to be possible by Wulfmeyer *et*

24 *al.* (2010) based on the use of the data from the Atmospheric Radiation Measurement (ARM) Raman

25 lidar operated at the Southern Great Plains Climate Research Facility site in Oklahoma (U.S.A.). The

26 same was demonstrated by Behrendt *et al.* (2015) for temperature turbulent fluctuations with rotational

27 Raman lidar. To the best of our knowledge, *BASIL* is the first Raman lidar system demonstrating the

28 capability to simultaneously measure profiles of water vapour and temperature turbulent fluctuations up

29 to the fourth order during daytime throughout the atmospheric CBL.

30 In the present paper a comprehensive assessment of the performances of the Raman lidar system *BASIL*

31 has been also carried out. Noise error profiles have been estimated based on the application of the auto-

32 covariance method and compared with the noise profiles estimated through Poisson statistics. The

Atmospheric
Chemistry
and Physics
Discussions

1   measurements of the higher-order moments of water vapour mixing ratio and temperature fluctuations

2   are characterized by very small sampling and noise errors, which make the quality of the present

3   turbulence measurements very high and demonstrates their capability to accurately observe the

4   structures present in the turbulent variables' profiles. In the determination of the temperature profiles,

5   particular care was dedicated in minimizing the potential systematic error associated with elastic signal

6   leakage in the rotational Raman signals. For this purpose, a specific algorithm was illustrated and tested,

7   which allowed to identify and remove signal leakages and to assess the residual systematic uncertainty

8   affecting temperature measurements after correction. In order to overcome the systematic uncertainty

9   associated with this correction, a future upgrade of *BASIL* is planned with the introduction of a new Lo-

10   J filter with high blocking at 354.7 nm and high center wavelength transmission to be developed

11   benefiting from the recent advances in multi-cavity interference filter technology.

12   Limited data is presently available in literature in terms of measurements or model simulations of

13   higher-order moments for both water vapour mixing ratio and temperature fluctuations. Consequently, a

14   deeper insight into possible interpretations of their vertical variability lacks of additional supporting

15   data. The availability of state-of-art rotational and vibrational Raman lidar systems capable to provide

16   high-resolution and accurate water vapour and temperature measurements will certainly help to fill this

17   gap, at least on the measurement side.

18   Future evolutions of this research work include the possibility to (i) compare - for a large variety of

19   clear sky cases collected during HOPE field campaign - the measurements of higher-order moments of

20   moisture and temperature fluctuations performed by *BASIL* with those simultaneously measured by the

21   University of Hohenheim water vapour DIAL and temperature rotational Raman lidar (located approx.

22   4 km E-SE), (ii) extend the analysis to cloud-topped CBLs from different field deployments, as in fact

23   important effect of clouds on turbulent exchange processes in the entrainment zone are expected to be

24   relevant, (iii) compare the measurements of higher-order moments of moisture and temperature

25   fluctuations from *BASIL* with estimates from large eddy simulation, and (iv) complement these studies

26   with a dedicated evaluation of the correlation between temperature and moisture.

27

Atmospheric
Chemistry
and Physics
Discussions

1   für Physik und Meteorologie, Universität Hohenheim, for their support in the collection and analysis of

2   the present data set.

3

4   **References**

5   Behrendt, A., and J. Reichardt: Atmospheric temperature profiling in the presence of clouds with a pure

6   rotational Raman lidar by use of an interference-filter-based polychromator, Appl. Opt., 39, 9, p. 1372-

7   1378, doi: 10.1364/AO.39.001372, 2000.

8   Behrendt, A., Nakamura, T., Onishi, M., Baumgart, R., and Tsuda, T.: Combined Raman lidar for the

9   measurement of atmospheric temperature, water vapor, particle extinction coefficient, and particle

10   backscatter coefficient, Appl. Optics, 41, 7657–7666, doi: 10.1364/AO.41.007657, 2002.

11   Behrendt, A.: Temperature Measurements with Lidar. In: C. Weitkamp (Ed.), Lidar: Range-Resolved

12   Optical Remote Sensing of the Atmosphere, Springer Series in Optical Sciences, Vol. 102, ISBN: 0-

13   387-40075-3, Springer, New York, 273-305, doi: 10.1007/0-387-25101-4_10, 2005.

14   Behrendt, A., Pal, S., Aoshima, F., Bender, M., Blyth, A., Corsmeier, U., Cuesta, J., Dick, G.,

15   Dorninger, M., Flamant, C., Di Girolamo, P., Gorgar, T., Huang, Y., Kalthoff, N., Khodayar, S.,

16   Mannstein, H., Träumner, K., Wieser, A., and Wulfmeyer, V.: Observations of convection initiation

17   processes with a suite of state-of-the-art research instruments during COPS IOP8b, Q. J. Roy. Meteor.

18   Soc., 137, 81–100, doi: 10.1002/qj.758, 2011a.

19   Behrendt, A., Pal, S., Wulfmeyer, V., Valdebenito B., Á. M., and Lammel, G.: A novel approach for the

20   char-acterisation of transport and optical properties of aerosol particles near sources, Part I:

21   measurement of particle backscatter coe_cient maps with a scanning UV lidar, Atmos. Environ., 45,

22   2795–2802, doi:10.1016/j.atmosenv.2011.02.061, 2011b.

23   Behrendt, A.,Wulfmeyer, V., Hammann, E, Muppa, S. K., and Pal, S.: Profiles of second to third order

24   moments of turbulent temperature fluctuations in the convective boundary layer: First measurements

25   with rotational Raman lidar, Atmos. Chem. Phys., 15, 5485-5500, DOI:10.5194/acp-15-5485-2015,

26   2015.

27   Bengtsson, L., Hodges, K. I., and Hagemann, S.: Sensitivity of the ERA40 reanalysis to the observing

28   system: determination of the global atmospheric circulation from reduced observations, Tellus A, 56,

29   456–471, doi:10.1111/j.1600-0870.2004.00079.x, 2004.

Atmospheric
Chemistry
and Physics
Discussions

1   Berg, L. K., Stull, R. B.: A simple parameterization coupling the convective daytime boundary layer
2   and fair-weather cumuli, J. Atmos. Sci., 62, 1976–1988, DOI: http://dx.doi.org/10.1175/JAS3437.1,
3   2005.

4   Bhawar, R., Di Girolamo, P., Summa, D., Flamant, C., Althausen, D., Behrendt, A., Kiemle, C., Bosser,
5   P., Cacciani, M., Champollion, C., Di Iorio, T., Engelmann, R., Herold, C., Pal, S., Riede, A., Wirth, M.,
6   and Wulfmeyer, V.: The Water vapour intercomparison effort in the framework of the convective and
7   orographically-induced precipitation study: air-borne-toground-based and airborne-to-airborne lidar
8   systems, COPS Special Issue, Q. J. Roy. Meteor. Soc., 137, 325–348, doi: 10.1002/qj.697, 2011.

9   Couvreux, F., Guichard, F., Redelsperger, J-L., Kiemle, C., Masson, V., Lafore, J-P., Flamant, C.:
10 Water-vapour velocity within a convective boundary layer assessed by large-eddy simulations and
11 IHOP_2002 observations. Q. J. Roy. Meteor. Soc., 131, 2665–2693, doi: 10.1256/qj.04.167, 2005.

12 Couvreux, F., Guichard, F., Masson, V., Redelsperger, J-L. : Negative water-vapour skewness and dry
13 tongues in the convective boundary layer: observations and large-eddy simulation budget analysis.
14 Boundary-Layer Meteorol., 123, 269-294, doi:10.1007/s10546-006-9140-y, 2007.

15 Dierer, S., Arpagaus, M., Seifert, A., Avgoustoglou, E., Dumitrache, R., Grazzini, F., Mercogliano, P.,
16 Milelli, M., and Starosta, K.: Deficiencies in quantitative precipitation forecasts: sensitivity studies
17 using the COSMO model, Meteorol. Z., 18, 631–645, doi:10.1127/0941-2948/2009/0420, 2009.

18 Di Girolamo, P., R. V. Gagliardi, G. Pappalardo, N. Spinelli, R. Velotta, V. Berardi: Two wavelength
19 Lidar analysis of stratospheric aerosol size distribution, J. Aerosol Sci., 26, 989-1001, ISSN: 0021-8502,
20 doi: 10.1016/0021-8502(95)00025-8, 1995.

21 Di Girolamo, P., P. F. Ambrico, A. Amodeo, A. Boselli, G. Pappalardo, N. Spinelli: Aerosol
22 observations by Lidar in the Nocturnal Boundary Layer, App. Opt., 38, 4585-4595, ISSN: 0003-6935,
23 doi: 10.1364/AO.38.004585, 1999.

24 Di Girolamo, P., Marchese, R., Whiteman, D. N., Demoz B. B.: Rotational Raman Lidar measurements
25 of atmospheric temperature in the UV. Geophys. Res. Lett., 31, L01106, ISSN: 0094-8276, doi:
26 10.1029/2003GL018342, 2004.

27 Di Girolamo, P., Behrendt, A., and Wulfmeyer, V.: Spaceborne profiling of atmospheric temperature
28 and particle extinction with pure rotational Raman Lidar and of relative humidity in combination with
29 differential absorption Lidar: performance simulations. Appl. Opt., 45, 2474-2494, doi:
30 10.1364/AO.45.002474, 2006.

Atmospheric
Chemistry
and Physics
Discussions

1   Di Girolamo, P., Behrendt, A., Kiemle, C., Wulfmeyer, V., Bauer, H., Summa, D., Dornbrack, A., Ehret,

2   G.: Simulation of satellite water vapour lidar measurements: Performance assessment under real

3   atmospheric conditions. Rem. Sens. Environ., 112, 1552-1568, doi: 10.1016/j.rse.2007.08.008, 2008.

4   Di Girolamo, P., Summa, D., Ferretti, R.: Multiparameter Raman Lidar Measurements for the

5   Characterization of a Dry Stratospheric Intrusion Event. J. Atm. Ocean. Tech., 26, 1742-1762, doi:

6   10.1175/2009JTECHA1253.1, 2009a.

7   Di Girolamo, P., D. Summa, R. F. Lin, T. Maestri, R. Rizzi, G. Masiello: UV Raman lidar

8   measurements of relative humidity for the characterization of cirrus cloud microphysical properties,

9   Atmos. Chem. Phys., 9, 8799-8811, 2009b. doi:10.5194/acp-9-8799-2009, 2009b.

10   Di Girolamo, P., D. Summa, R. Bhawar, T. Di Iorio, M. Cacciani, I. Veselovskii, O. Dubovik, A.

11   Kolgotin: Raman lidar observations of a Saharan dust outbreak event: Characterization of the dust

12   optical properties and determination of particle size and microphysical parameters, Atmos. Envir., 50,

13   66-78, 2012a. doi: 10.1016/j.atmosenv.2011.12.061, 2012a.

14   Di Girolamo, P., D. Summa, M. Cacciani, E. G. Norton, G. Peters, Y. Dufournet: Lidar and radar

15   measurements of the melting layer: observations of dark and bright band phenomena, Atmos. Chem.

16   Phys., 12, 4143-4157, 2012b.doi: 10.5194/acp-12-4143-2012, 2012b.

17   Di Girolamo, P., C. Flamant, M. Cacciani, E. Richard, V. Ducrocq, D. Summa, D. Stelitano, N. Fourrié

18   and F. Saïd, Observation of low-level wind reversals in the Gulf of Lion area and their impact on the

19   water vapour variability, Q. J. Roy. Meteor. Soc., doi: 10.1002/qj.2767, 2016a.

20   Di Girolamo, P., Cacciani, D., Scoccione, A., Summa, D., Turner, D. D., Wulfmeyer, V., Schween, J.

21   H., Crewell, S.: Deployment of the of the Raman lidar system BASIL in the frame of the HD(CP)2

22   Observational Prototype Experiment – HOPE: upgrades of the instrument to fulfil the aims of the

23   experiment and overview of the performed measurements, in preparation, to be submitted for

24   publication in Atmos. Chem. Phys, 2016b.

25   Eberhard, W. L., Cupp, R. E., Healy, K. R.: Doppler lidar measurement of profiles of turbulence and

26   momentum flux. J. Atm. Ocean. Tech., 6, 809–819, DOI: http://dx.doi.org/10.1175/1520-

27   0426(1989)006<0809:DLMOPO>2.0.CO;2, 1989.

28   Frehlich, R., and Cornman, L.: Estimating spatial velocity statistics with coherent Doppler lidar. J. Atm.

29   Ocean. Tech., 19, 355–366, DOI: http://dx.doi.org/10.1175/1520-0426-19.3.355, 2002.

30   Garratt, J. R.: The Atmospheric Boundary Layer, Cambridge Atmospheric and Space Science Series,

31   pages 336, ISBN: 9780521467452, 1992.

Atmospheric
Chemistry
and Physics
Discussions

Open Access

EGU

1   Griaznov, V., I. Veselovskii, P. Di Girolamo, M. Korenskii, D. Summa: Spatial distribution of doubly

2   scattered polarized laser radiation in the focal plane of a lidar receiver, Appl. Opt., 46, 6821–6830, doi:

3   10.1364/AO.46.006821, 2007.

4   Gustafson, W. I. Jr, and Berg, L. K.: Implementation of the probabilistic CuP cumulus parameterization

5   in WRF. In: 8th annual WRF user's workshop, Boulder, USA, June 11–15, 2007.

6   Hammann, E., Behrendt, A., Le Mounier, F., and Wulfmeyer, V.: Temperature profiling of the

7   atmospheric boundary layer with rotational raman lidar during the HD(CP)2 5 observational prototype

8   experiment, Atmos. Chem. Phys., 15, 2867-2881, doi:10.5194/acp-15-2867-2015, 2015a.

9   Hammann, E., A. Behrendt, V. Wulfmeyer: Recent upgrades of the rotational Raman lidar of the

10   University of Hohenheim for the measurement of temperature profiles in the surface layer. Reviewed

11   extended abstracts of the 27th International Laser Radar Conference (ILRC27), paper #249, New York

12   City, USA, July 5 - 10, 2015b.

13   Kalthoff, N., M. Kohler, C. Barthlott, B. Adler, S. D. Mobbs, U. Corsmeier, K. Träumner, T. Foken, R.

14   Eigenmann, L. Krauss, S. Khodayar, P. Di Girolamo: The dependence of convection-related parameters

15   on surface and boundary-layer conditions over complex terrain. Q. J. Roy. Meteor. Soc., 137, 70-80,

16   ISSN: 0035-9009, doi: 10.1002/qj.686, 2011.

17   Kiemle, C., Ehret, G., Giez, A., Davis, K. J., Lenschow, D. H., and Oncley, S. P.: Estimation of

18   boundary layer humidity fluxes and statistics from airborne DIAL. J. Geophys. Res., 102 (D24), 29

19   189–29 204, doi: 10.1029/97JD01112, 1997.

20   Kiemle, C., Brewer, W. A., Ehret, G., Hardesty, R. M., Fix A., Senff, C.,Wirth, M., Poberaj G., LeMone,

21   M. A.: Latent heat flux profiles from collocated airborne water vapour and wind lidars during

22   IHOP_2002. J. Atm. Ocean. Tech., 24, 627–639, DOI: http://dx.doi.org/10.1175/JTECH1997.1, 2007.

23   Lenschow, D. H., and Kristensen, L.: Uncorrelated noise in turbulence measurements. J. Atm. Ocean.

24   Tech., l2, 68–81, DOI: http://dx.doi.org/10.1175/1520-0426(1985)002<0068:UNITM>2.0.CO;2, 1985.

25   Lenschow, D. H.,Wulfmeyer., V., Senff, C., Measuring second-through fourth-order moments in noisy

26   data. J. Atm. Ocean. Tech., 17, 1330–1347, doi:10.1175/1520-0426(2000)0172.0.CO;2, 2000.

27   Mahrt, L.: Boundary-layer moisture regimes. Q. J. Roy. Meteorol. Soc. 117:151–176,

28   DOI: 10.1002/qj.49711749708, 1991.

Atmospheric
Chemistry
and Physics
Discussions

Open Access

EGU

1   McNicholas, C., and Turner, D. D.: Characterizing the convective boundary layer turbulence with a

2   High Spectral Resolution Lidar, J. Geophys. Res. Atmos., 119, 12,910–12,927,

3   doi:10.1002/2014JD021867, 2014.

4   Milovac, J., Warrach-Sagi, K., Behrendt, A., Späth, F., Ingwersen, J., and Wulfmeyer, V.: Investigation

5   of PBL schemes combining the WRF model simulations with scanning water vapour differential

6   absorption lidar measurements. J. Geophys. Res. Atmos. 121 (2), 624–649,

7   DOI :10.1002/2015JD023927, 2016.

8   Muppa, S.K., Behrendt, A., Späth, F., Wulfmeyer, V., Metzendorf, S., and Riede, A.: Turbulent

9   humidity fluctuations in the convective boundary layer: Case studies using water vapour differential

10 absorption lidar measurements, Bound.-Lay. Meterorol., 58 (1), 43-66. DOI:10.1007/s10546-015-0078-

11 9, 2016.

12 Newsom, R. K, Turner, D. D., Mielke, B., Clayton, M., Ferrare, R., Sivaraman, C.: The use of

13 simultaneous analog and photon counting detection for Raman lidar. Appl. Opt., 48, 3903–3914,

14 doi: 10.1364/AO.48.003903, 2009.

15 Nocera, R., Raman lidar measurements of the atmospheric temperature vertical profile, Master Thesis,

16 Potenza, 2016.

17 Pal, S., Behrendt, A. and Wulfmeyer, V.: Elastic-backscatter lidar based characteri-zation of the

18 convective boundary layer and investigation of related statistics, Ann. Geophys. 28, 825-847,

19 DOI:10.5194/angeo-28-825-2010, 2010.

20 Radlach, M., Behrendt, A., and Wulfmeyer, V.: Scanning rotational Raman lidar at 355 nm for the

21 measurement of tropospheric temperature fields, Atmos. Chem. Phys., 8, 159–169, doi:10.5194/acp-8-

22 159-2008, 2008.

23 Senff, C., Bösenberg, J., Peters, G., Schaberl, T.: Remote sensing of turbulent ozone fluxes and the

24 ozone budget in the convective boundary layer with DIAL and radar-RASS: a case study, *Contrib.*

25 *Atmos. Phys.*, 69, 161–176, 1996.

26 Sorbjan, Z.: Effects caused by varying the strength of the capping inversion based on a large eddy

27 simulation model of the shear-free convective boundary layer. J Atmos Sci., 53, 2015-2024, 1996.

28 Späth, F., Metzendorf, S., Behrendt, A., Wizemann, H. D., Wagner, G., and Wulfmeyer, V.:

29 Online/offline injection seeding system with high frequency-stability and low crosstalk for water vapor

30 DIAL, Opt. Commun., 309, 37–43, doi:10.1016/j.optcom.2013.07.003, 2013.

Atmospheric
Chemistry
and Physics
Discussions

Späth, F., A. Behrendt, S. K. Muppa, S. Metzendorf, A. Riede, and V. Wulfmeyer: 3D water vapor field in the atmospheric boundary layer observed with scanning differential absorption lidar. Atmos. Meas. Tech., 9, 1701-1720, doi:10.5194/amt-9-1701-2016, 2016.

Stull, R. B.: An Introduction to Boundary Layer Meteorology, Atmospheric Sciences Library, 1988.

Su, J., McCormick, M. P.,Wu, Y., Lee III, R. B., Lei, L., Liu, Z., and Leavor, K. R.: Cloud temperature measurement using rotational Raman lidar, J. Quant. Spectrosc. Ra., 125, 45–50, 2013.

Sullivan P.P., Moeng C-H., Stevens B., Lenschow D.H., Mayor S.D.: Structure of the entrainment zone capping the convective atmospheric boundary layer. J Atmos Sci., 55, 3042–3064, 1998.

Summa, D., Di Girolamo, P., Stelitano, D., Cacciani, M.: Characterization of the planetary boundary layer height and structure by Raman Lidar: Comparison of different approaches, Atmos. Meas. Tech., 6, 3515-3525, doi: 10.5194/amt-6-3515-2013, 2013.

Turner, D.D., Wulfmeyer, V., Berg, L.K., and Schween, J.H.: Water vapor turbulence profiles in stationary continental convective mixed layers, J. Geophys. Res. 119, 11,151-11,165, DOI:10.1002/2014JD022202, 2014a.

Turner, D. D., Ferrare, R. A., Wulfmeyer, V., and Scarino, A. J.: Aircraft evaluation of ground-based Raman lidar water vapor turbulence profiles in convective mixed layers. J. Atmos. Oceanic Technol., 31, 1078–1088, doi:10.1175/JTECH–D–13–00 075.1, 2014b.

Wagner, G., V. Wulfmeyer, F. Späth, A. Behrendt, and M. Schiller: Performance and specifications of a pulsed high-power single-frequency Ti:Sapphire laser for water-vapor differential absorption lidar. Appl. Opt. 52, 2454-2469, doi: 10.1364/AO.52.002454, 2013.

Whiteman, D. N.: Examination of the traditional Raman lidar technique. I. Evaluating the temperature-dependent lidar equations, Appl. Opt., 42, 2571-2592, doi: 10.1364/AO.42.002571, 2003.

Wulfmeyer, V.: Investigation of turbulent processes in the lower troposphere with water-vapour DIAL and radar-RASS. J. Atmos. Sci., 56, 1055–1076, doi: http://dx.doi.org/10.1175/1520-0469(1999)056<1055:IOTPIT>2.0.CO;2, 1999a.

Wulfmeyer, V.: Investigations of humidity skewness and variance profiles in the convective boundary layer and comparison of the latter with large eddy simulation results. J. Atmos. Sci., 56, 1077–1087, doi: http://dx.doi.org/10.1175/1520-0469(1999)056<1077:IOHSAV>2.0.CO;2 ,1999b.

Wulfmeyer, V., *et al.*: RESEARCH CAMPAIGN: THE CONVECTIVE AND OROGRAPHICALLY INDUCED PRECIPITATION STUDY A Research and Development Project of the World Weather

Atmospheric
Chemistry
and Physics
Discussions

Open Access

EGU

1 Research Program for Improving Quantitative Precipitation Forecasting in Low-Mountain Regions.

2 Bulletin of the American Meteorological Society, 89, 1477-1486, ISSN: 0003-0007, doi:

3 10.1175/2008BAMS2367.1, 2008.

4 Wulfmeyer, V., Turner, D. D., Pal, S., and Wagner, E.: Can water vapour raman lidar resolve profiles of

5 turbulent variables in the convective boundary layer?, Bound.-Lay. Meteorol., 136, 253-284,

6 doi:10.1007/s10546-010-9494-z, 2010.

7 Wulfmeyer, V., Hardesty, M., Turner, D.D., Behrendt, A., Cadeddu, M., Di Girolamo, P., Schlüssel, P.,

8 van Baelen, J., and Zus, F.: A review of the remote sensing of lower-tropospheric thermodynamic

9 profiles and its indispensable role for the understanding and the simulation of water and energy cycles,

10 Rev. Geophys., 53, 819–895, DOI:10.1002/2014RG000476, 2015.

11 Wulfmeyer, V., Muppa, S., Behrendt, A., Hammann, E., Späth, F., Sorbjan, Z., Turner, D.D., and

12 Hardesty, R.M.: Determination of convective boundary layer entrainment fluxes, dissipation rates, and

13 the molecular destruction of variances: Theoretical description and a strategy for its confirmation with a

14 novel lidar system synergy, J. Atmos. Sci., 73 (2), 667-692, doi: 10.1175/JAS-D-14-0392.1, 2016.

15

Atmospheric
Chemistry
and Physics
Discussions

Open Access

1   **Figures captions**
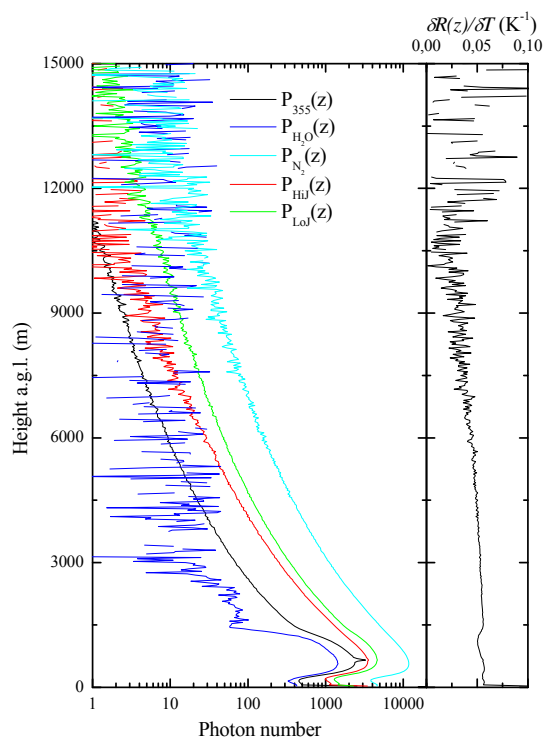
2   **Figure 1:** Profiles of noise error affecting water vapour mixing ratio (panels a and b) and temperature

3   (panel c) measurements The figure illustrates the estimates determined based on the application of the

4   auto-covariance method, obtained by extrapolating the structure function to lag zero, and the error

5   profiles obtained based on the application of Poisson statistics to signal photon counts.
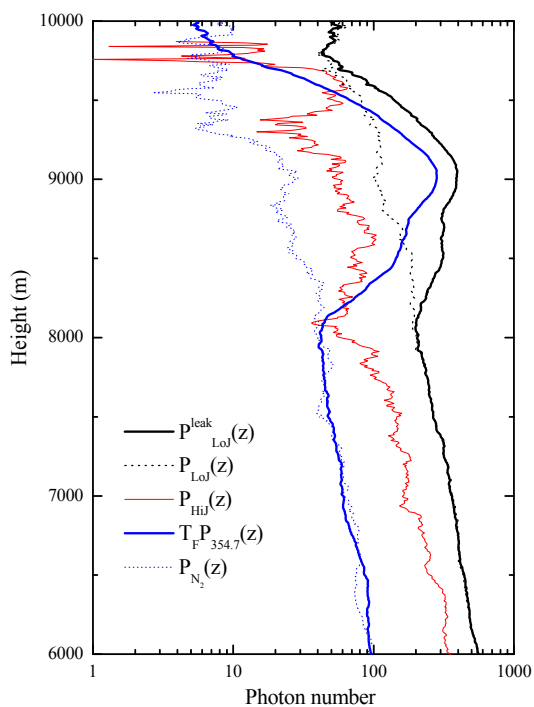
6   Time-height cross-section of the particle backscatter coefficient, β_{par}, between 11:30 and 13:30 UTC on

7   20 April 2013. The black line in the figure identifies the CBL height z_i.

8   **Figure 2:** (panel a) The mean photon numbers (10 sec average) for the considered signals, i.e. the water

9   vapour and molecular nitrogen vibrational Raman signals, $P_{H_2O}(z)$ and $P_{N_2}(z)$, the 355 nm elastic

10   signal, $P_{355}(z)$, and the pure-rotational Raman signals, $P_{LoJ}(z)$ and $P_{HiJ}(z)$; (panel b) temperature

11   sensitivity of RRL measurement technique. $\partial R(z)/\partial T$.

12   **Figure 3**: Vertical profiles of $P_{LoJ}^{leak}(z)$, $P_{HiJ}(z)$, $T_F\, P_{354.7}(z)$ and $P_{LoJ}^{synt}(z)$ for the time interval 13:38-13:46

13   UTC on 20 April 2013, revealing the presence of high cirrus clouds extending between 7.9 and 9.8 km.

14   **Figure 4**: Time-height cross-section of the particle backscatter coefficient, β_{par}, between 11:30 and

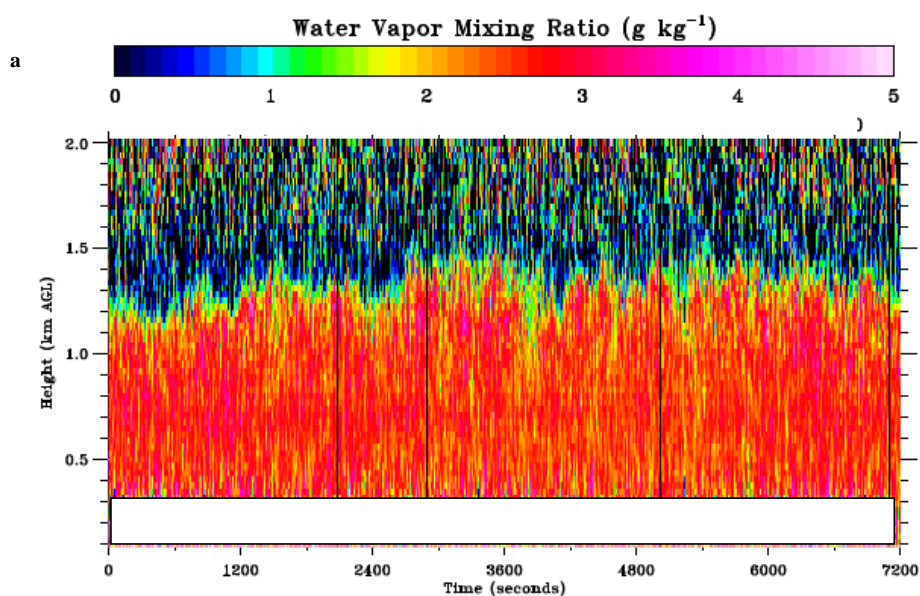15   13:30 UTC on 20 April 2013. The black line in the figure identifies the CBL height z_i.

16   **Figure 5:** Time-height cross section of water vapour mixing ratio (panel a) and temperature (panel b) in

17   the same time interval considered in figure 4.

18   **Figure 6:** Mean water vapour mixing ratio (panel a) and temperature (panel b) profiles measured by

19   *BASIL* on 20 April 2013 between 11:30 and 13:30 UTC, together with the corresponding profiles as

20   measured by a radiosonde launched at 13:00 UTC from the nearby site of Hambach. Noise error bars

21   are also shown.

22   **Figure 7:** Time-height cross section of water vapour mixing ratio (panel a) and temperature fluctuations

23   (panel b) in the same time interval considered in figure 4.

24   **Figure 8:** Auto-covariance functions obtained from the measured water vapour mixing ratio (panel a)

25   and temperature (panel b) fluctuations in the same time interval considered in figure 4. Auto-covariance

26   functions are displayed for the height levels between 400 and 1600 m a.g.l., i.e., 0.3 to 1.25 z_i, for lags

27   from -200 to 200 s.

28   **Figure 9:** Integral scale of water vapour mixing ratio (panel a) and temperature fluctuations (panel b)

29   computed for the same time interval considered in figure 4.

Atmospheric
Chemistry
and Physics
Discussions

1   **Figure 10**: Vertical profiles of atmospheric and total variance for water vapour mixing ratio (panel a)

2   and temperature (panel b) computed for the same time interval considered in figure 4. In the figure the

3   error bars represent only the noise error.

4   **Figure 11**: Vertical profiles of the third-order moment for water vapour mixing ratio (panel a) and

5   temperature (panel b) computed for the same time interval considered in figure 4. In the figure the error

6   bars represent only the noise error.

7   **Figure 12**: Vertical profiles of the fourth-order moment for water vapour mixing ratio (panel a) and

8   temperature (panel b) computed for the same time interval considered in figure 4. In the figure the error

9   bars represent only the noise error.

10   **Figure 13**: Vertical profiles of skewness (panel a) and kurtosis (panel b) for water vapour mixing ratio

11   and temperature computed for the same time interval considered in figure 4. In the figure the thick error

12   bars represent the noise error, while the thin error bars represent the sampling error.

13

1

2

Atmospheric
Chemistry
and Physics
Discussions

Open Access

EGU

Figure 1: Profiles of noise error affecting water vapour mixing ratio (panels a and b) and temperature (panel c) measurements The figure illustrates the estimates determined based on the application of the auto-covariance method, obtained by extrapolating the structure function to lag zero, and the error profiles obtained based on the application of Poisson statistics to signal photon counts.

1

Figure 2: (panel a) The mean photon numbers (10 sec average) for the considered signals, i.e. the water vapour and molecular nitrogen vibrational Raman signals, $P_{H_2O}(z)$ and $P_{N_2}(z)$, the 355 nm elastic signal, $P_{355}(z)$, and the pure-rotational Raman signals, $P_{LoJ}(z)$ and $P_{HiJ}(z)$; (panel b) temperature sensitivity of RRL measurement technique. $\partial R(z)/\partial T$.

6

1

Figure 3: Vertical profiles of $P_{LoJ}^{leak}(z)$, $P_{HiJ}(z)$, $T_F P_{354.7}(z)$ and $P_{LoJ}^{synt}(z)$ for the time interval 13:38-13:46

3   UTC on 20 April 2013, revealing the presence of high cirrus clouds extending between 7.9 and 9.8 km.

4

Atmospheric
Chemistry
and Physics
Discussions

1
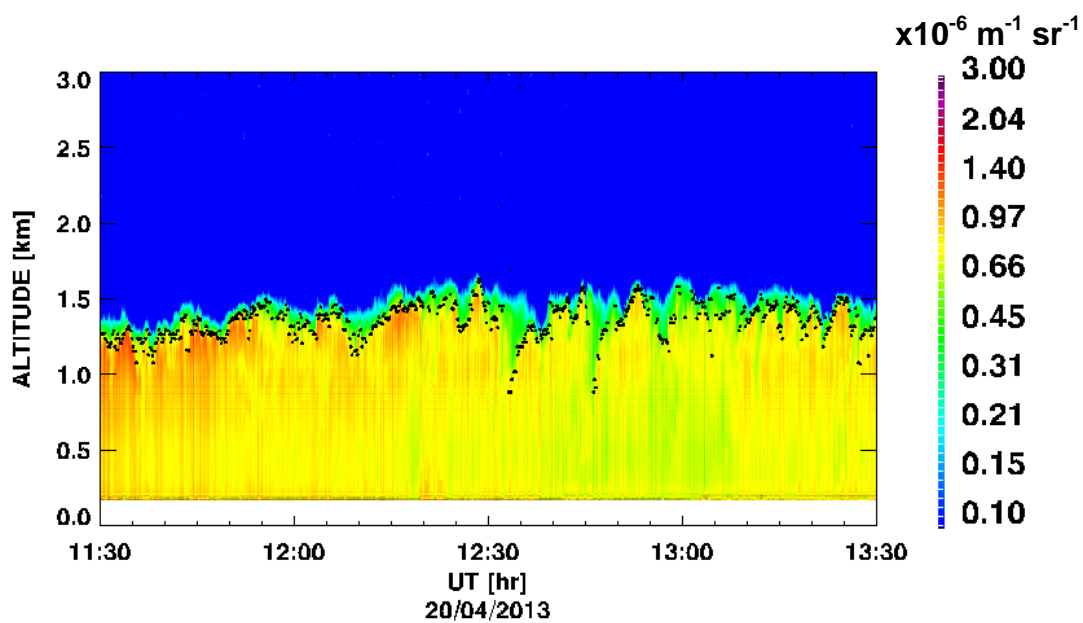
2
3   **Figure 4:** Time-height cross-section of the particle backscatter coefficient, β_{par}, between 11:30 and

4   13:30 UTC on 20 April 2013. The black line in the figure identifies the CBL height z_i.

5

1

2
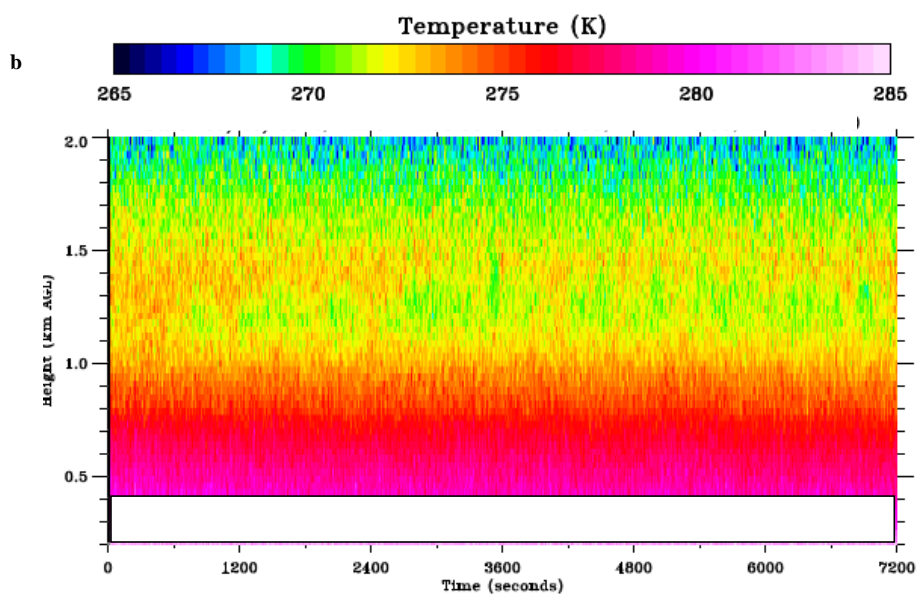
3

4 **Figure 5:** Time-height cross section of water vapour mixing ratio (panel a) and temperature (panel b) in
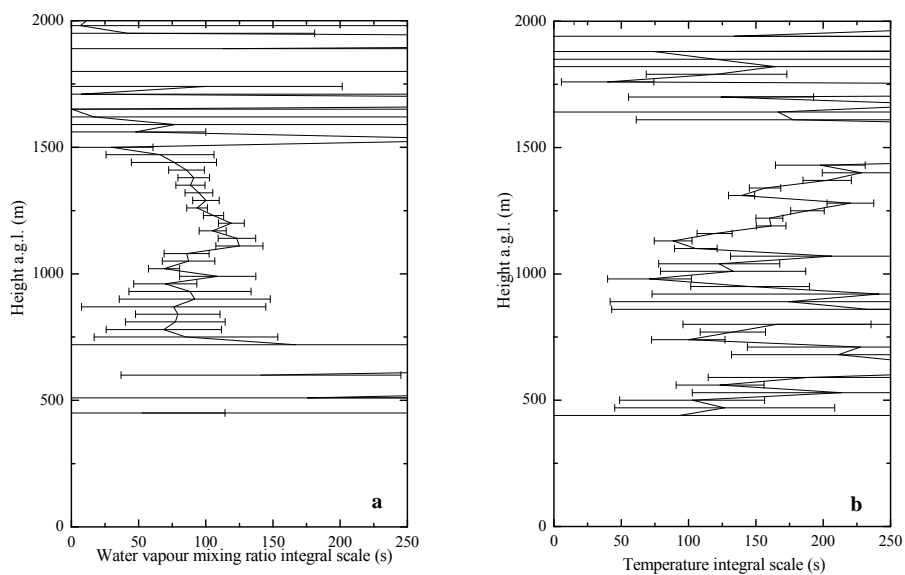
5 the same time interval considered in figure 4.
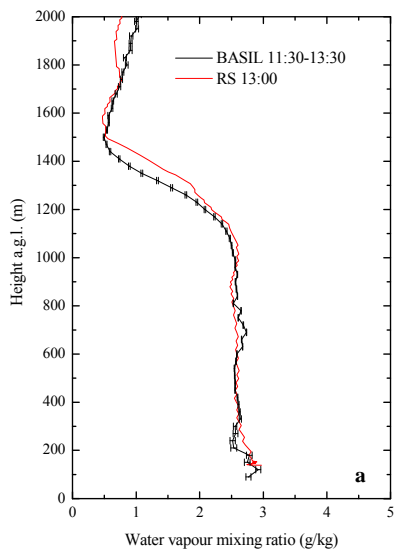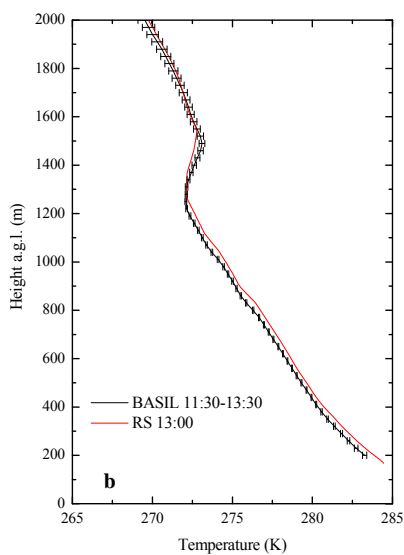
6

Atmospheric
Chemistry
and Physics
Discussions

1

2

3

4

Figure 6: Mean water vapour mixing ratio (panel a) and temperature (panel b) profiles measured by *BASIL* on 20 April 2013 between 11:30 and 13:30 UTC, together with the corresponding profiles as measured by a radiosonde launched at 13:00 UTC from the nearby site of Hambach. Noise error bars are also shown.

9

1

2

3

Figure 7: Time-height cross section of water vapour mixing ratio (panel a) and temperature fluctuations

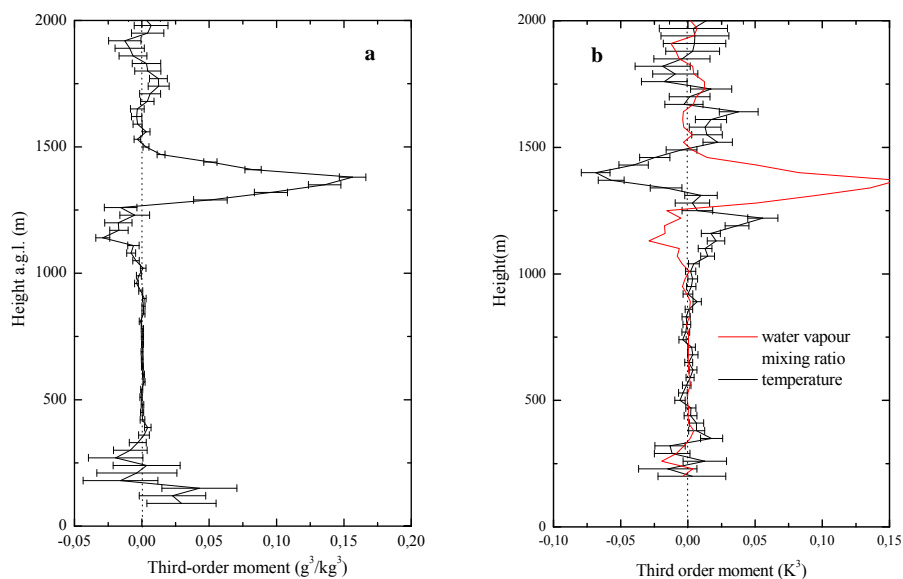(panel b) in the same time interval considered in figure 4.

6

Figure 8: Auto-covariance functions obtained from the measured water vapour mixing ratio (panel a) and temperature (panel b) fluctuations in the same time interval considered in figure 4. Auto-covariance functions are displayed for the height levels between 400 and 1600 m a.g.l., i.e., 0.3 to 1.25 z_i, for lags from -200 to 200 s.

1

2   **Figure 9:** Integral scale of water vapour mixing ratio (panel a) and temperature fluctuations (panel b)

3   computed for the same time interval considered in figure 4.

4

Atmospheric
Chemistry
and Physics
Discussions

1

2
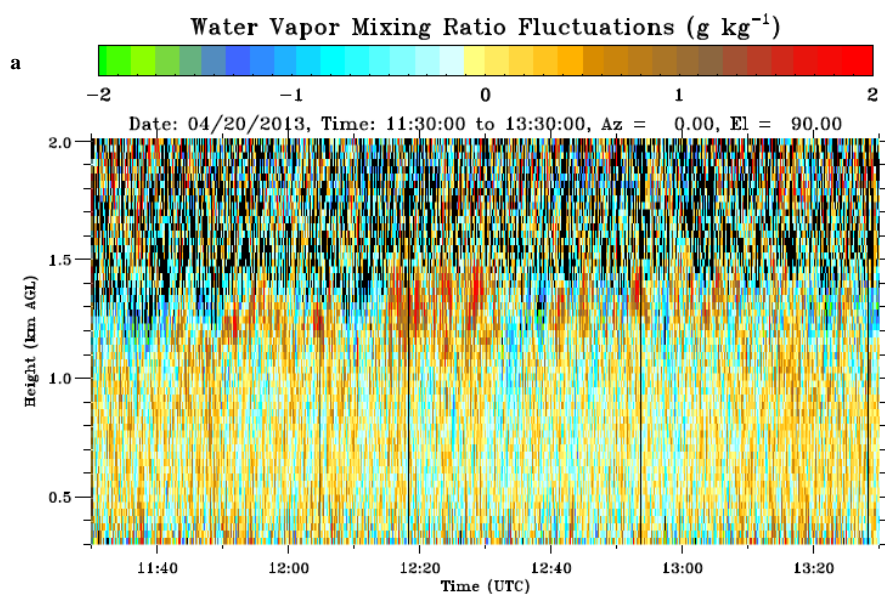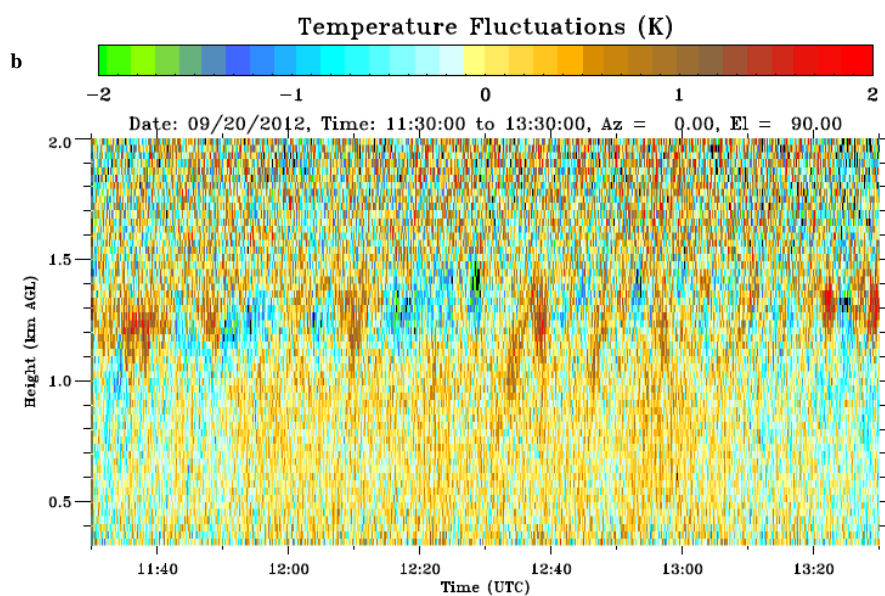
3 **Figure 10**: Vertical profiles of atmospheric and total variance for water vapour mixing ratio (panel a)

4 and temperature (panel b) computed for the same time interval considered in figure 4. In the figure the
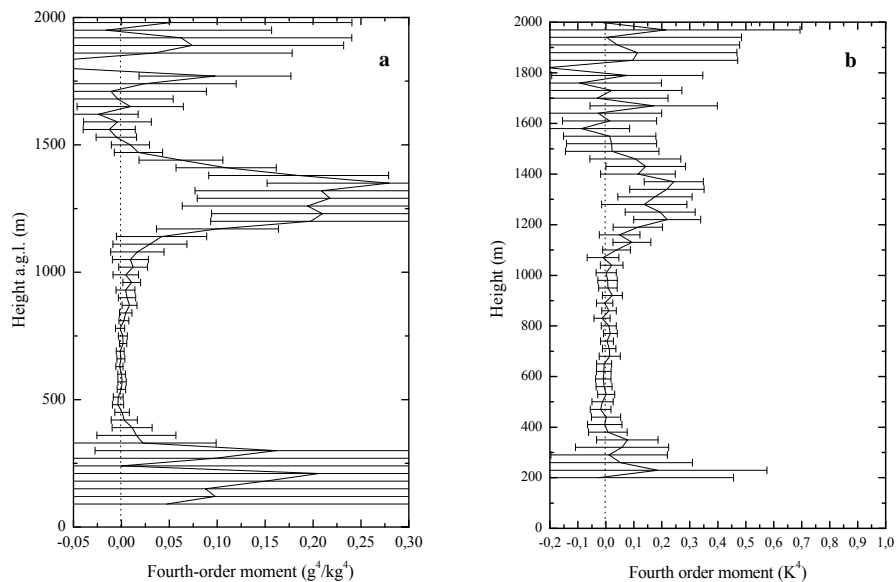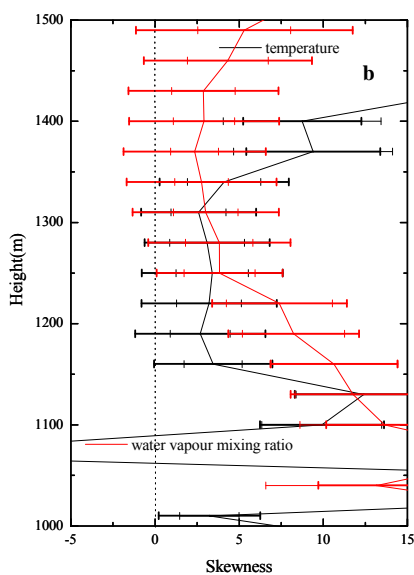
5 error bars represent only the noise error.

6

7

Atmospheric
Chemistry
and Physics
Discussions

1

Figure 11: Vertical profiles of the third-order moment for water vapour mixing ratio (panel a) and

temperature (panel b) computed for the same time interval considered in figure 4. In the figure the error
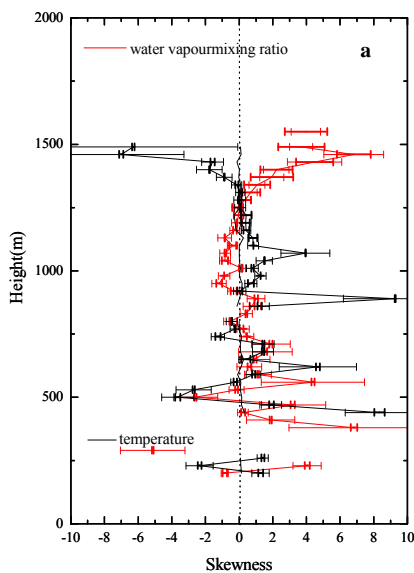
bars represent only the noise error.

5

1

2

Figure 12: Vertical profiles of the fourth-order moment for water vapour mixing ratio (panel a) and
temperature (panel b) computed for the same time interval considered in figure 4. In the figure the error
bars represent only the noise error.

6

Figure 13: Vertical profiles of skewness (panel a) and kurtosis (panel b) for water vapour mixing ratio
and temperature computed for the same time interval considered in figure 4. In the figure the thick error
bars represent the noise error, while the thin error bars represent the sampling error.